UNIVERSIDAD DE CONCEPCIÓN
FACULTAD DE CIENCIAS FÍSICAS Y MATEMÁTICAS

FORMACIÓN DE AGUJEROS NEGROS A TRAVÉS DE COLISIONES DE ESTRELLAS DE LA SECUENCIA PRINCIPAL EN CÚMULOS PRIMORDIALES CON UN POTENCIAL DE FONDO (FORMATION OF BLACK HOLES VIA COLLISIONS OF MAIN-SEQUENCE STARS IN PRIMORDIAL CLUSTERS WITH A BACKGROUND POTENTIAL)

Por: Kirsty Sehlke Abarca

Tesis presentada a la facultad de ciencias físicas y matemáticas de la Universidad de Concepción para optar al grado académico de Magíster en Ciencias con Mención en Física.

Abril 2023

Concepción, Chile

Profesor Guía: Dominik Schleicher - UdeC

Dedicada a mi madre Mariana Abarca Oyarzún

AGRADECIMIENTOS

Primero quiero comenzar agradeciendo a mi hermosa madre Mariana Abarca Oyarzún quien fue la persona que sembró un montón de semillitas en mi y las fue regando por mi hasta que yo pude regarlas por mi misma. Ella me mostró su amor por las matemáticas siendo una excelente Ingeniera de ejecución en mecánica y fue con su ejemplo que me he convertido en la mujer que soy hoy en día. Ella fue la que seco mis lágrimas cada vez que quise rendirme, aplaudió y se emociono conmigo en cada uno de mis triunfos y fue, es y seguirá siendo hasta mi ultimo día el motor que impulsa mis sueños. Gracias mama porque me mostraste que nada de lo que uno quiera alcanzar es imposible si te propones obtenerlo. Gracias porque aun yo sin creer en mi tu si creías en mi y a través de tus ojos yo podía verlo. Yo se que tu estabas muy orgullosa de mi y de ver todo ese camino que he recorrido de tu mano. Ahora tu sueltas mi mano físicamente y me dejas volar sola poniendo en practica cada una de las enseñanzas que me dejaste para el presente y el futuro pero no dudo que me seguirás apoyando desde el cielo. Gracias por ser mi madre, mi compañera, mi guía y por mostrarme como se siente ser amada incondicionalmente y haberme dado el honor de acompañarte en los últimos años de tu vida que se no fue fácil. Te extraño muchísimo y como te dije una de las ultimas veces que hablamos: "Mujeres fuertes inspiran niñas fuertes" y eso fuiste para mi la mujer mas fuerte que he conocido. Te amo mama. Ella con el dolor de mi alma falleció (21 de mayo de 1951 - 4 de noviembre del 2021) durante mi segundo año de magíster y porque se que así ella lo hubiese querido termine este magíster por ella.

Quiero también agradecer a mis tres mejores amigas de hace casi una década que han estado conmigo incondicionalmente que ahora son mi familia en especial en este ultimo tiempo que ha sido tan difícil para mi.

Agradecer a mis compañeros y compañeras de universidad con los cuales pude trabajar a la par independientemente de ser mujer en un campo mayoritariamente compuestos por hombres y por esas largas noches de estudios y cervezas que las hicieron mucho mas entretenidas con su compañia.

Por otro lado quiero agradecer a mi profesor guía Dominik Schleicher por dejarme formar parte de este grupo de agujeros negros, por ser un excelente profesor guía

y por el apoyo y comprensión que me dio en el que seguro va a ser el momento mas difícil de mi vida. También quiero agradecer a mi otro profesor guía Andrés Escala por siempre estar presente para explicar y guiar de muy buena manera mi investigación en complemento de la suya.
Finalmente agradecerle a la Universidad de Concepción por la beca que obtuve para realizar mi magíster en conjunto con mi titulo de pregrado a través de la beca de articulación y al soporte financiero a ANID con el proyecto Millenium Nucleus NCN19_058 (TITANs), que permite explorar de diversas formas los agujeros negros supermasivos desde su formación, crecimiento, características y tecnologías, por la beca que obtuve durante todo el proceso que duro el trabajo de esta investigación que se presenta a continuación.

Resumen

La asombrosa existencia de agujeros negros supermasivos en el Universo primitivo es uno de los grandes misterios sin respuesta en astrofísica, en particular, cómo obtienen sus grandes masas tan rápido. Aquí nuestro interés consiste en explorar un nuevo escenario de formación de agujeros negros masivos: la formación por colisiones estelares catastróficas en cúmulos estelares densos. Nuestros sistemas están localizados en el universo temprano, con las denominadas estrellas de población III las cuales son muy masivas y, por tanto, cúmulos de estrellas de población III son sistemas estelares muy densos y masivos. Las simulaciones de N cuerpos fueron corridas con el código *NBODY6++GPU* y pueden ser divididas en dos grupos, uno con potencial de fondo y otro sin potencial de fondo. Se ha establecido una masa crítica para la cual el número de colisiones es tan alto que puede llegar a formar agujeros negros masivos al interior de estos cúmulos estelares nucleares. Aquí, nuestro objetivo es testear la existencia de esta masa crítica en un caso simplificado de cúmulos de estrellas de población III de igual masa. En términos de la eficiencia para la formación de un objeto masivo, encontramos que ocurre una transición, ya que la eficiencia es muy pequeña para masas considerablemente por debajo del valor de masa crítica, alcanzando valores de $\sim 20\%$ una vez que comenzamos a acercarnos a la escala de masa crítica en nuestras simulaciones. Nuestros resultados sugieren que ocurre una transición crítica dependiendo de la masa del cúmulo y los objetos más masivos alcanzan masas de aproximadamente 1.7×10^5M.

Keywords – agujeros negros: formación – universo temprano – cúmulos estelares densos – colisiones estelares catastróficas – simulaciones

Abstract

The amazing existence of supermassive black holes in the primitive Universe is one of the great mysteries without answer in astrophysics, in particular, how they get their great masses so fast. Here our interest consists in exploring a new scenario for the formation of massive black holes: the formation by catastrophic stellar collisions in dense star clusters. Our systems are located in the early universe, with the so-called population III stars which are very massive, and therefore population III star clusters are very dense and massive stellar systems. The N-body simulations we run with the code *NBODY6++GPU* can be divided into two groups, one with background potential and the other without background potential. A critical mass has been established for which the number of collisions is so high that massive black holes can form within these nuclear star clusters. Here, our goal is to test the existence of this critical mass in a simplified case of population III star clusters of equal mass. In terms of the efficiency for the formation of a massive object, we find a transition to occur, as the efficiency is very small for masses considerably below the critical value while reaching values of $\sim 20\%$ once we start approaching the critical mass scale in our simulations. Our results thus suggest such a critical transition to occur depending on the mass of the cluster and the most massive objects reaching masses of about 1.7×10^5M.

Keywords – black hole: formation – early universe – dense stellar clusters – catastrophic stellar collsions – simulations

Contents

List of Tables

List of Figures

Chapter 1

Introduction

1.1 Supermassive black holes in the early universe

One of the most important questions in this field is: How did the first supermassive black holes (SMBHs) grow so large so fast? The answer is that the dominant formation pathway of SMBHs is still a mystery. The presence of SMBHs with masses greater than 10^9 $M_\odot$ when the Universe was a billion years old represents an intriguing puzzle. Some of the theories to answer this question are that very massive black hole seeds were formed, and that black holes (BHs) have grown extremely rapidly either via accretion of the surrounding gas at super Eddington rates or collisions with other smaller BHs. How are BHs thought to have formed? So far there are three theories of how these massive black holes (MBHs) formed. The first is the direct collapse of a primordial cloud, in which primordial clouds of interstellar gas collapse under self-gravity to form supermassive stars which then evolve into supermassive black holes. The second is growth by gas accretion. And the third is the formation of an MBH by catastrophic stellar collisions in dense stellar clusters.

A naive explanation (to the question we asked ourselves earlier) is that these early SMBHs were seeded by BH remnants of the first Population III stars. Pop III stars are expected to form in dark matter minihalos from primordial gas undergoing molecular hydrogen cooling. The metal-free primordial gas is significantly warmer (a few 100 K) than star-forming molecular clouds in the interstellar medium (ISM) in our Galaxy ($\approx$10 K). The general expectation is that inefficient cooling of the primordial gas leads to inefficient fragmentation, making Pop III stars unusually

massive (Inayoshi et al., 2020). Population III stars formed approximately 400 million years after the Big Bang as shown in the figure 1.1.1.

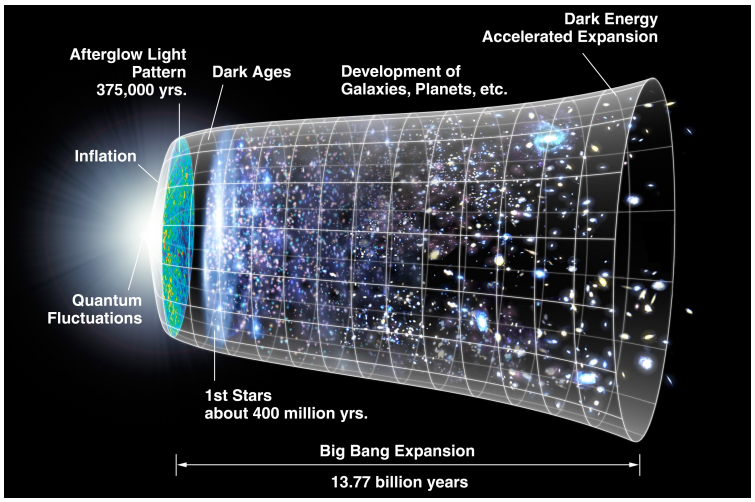

Figure 1.1.1: A representation of the evolution of the universe over 13.77 billion years. Source: (NASA / WMAP Science Team, 2006). See the page here https://map.gsfc.nasa.gov/media/060915/index.html.

The left side in figure 1.1.1 represents the earliest time in the universe that we can now probe when a period of "inflation" produced a burst of exponential growth in the universe. (The size is represented by the vertical extent of the grid in this graphic.) Over the next few billion years, the expansion of the universe gradually slowed down as the matter in the universe attracted itself through gravity. In recent times, the expansion began to speed up again as the repulsive effects of dark energy started to dominate the expansion of the universe. In the figure, you can also see the Wilkinson Microwave Anisotropy Probe (WMAP), a NASA spacecraft operating from 2001 to 2010 which measured the temperature differences across the sky in the cosmic microwave background (CMB), the radiant heat remaining from the Big Bang. The residual light seen by WMAP was emitted about 375,000 years after inflation and has traversed the universe largely unhindered ever since. The conditions of previous times are imprinted in this light and it is in this way that we can study it; it also forms a backlight for later developments in the universe.

In figure 1.1.2 you can see the different possible paths of black hole formation that are studied today. Each with different objects and under different conditions. To explain the formation of supermassive black holes, intermediate-mass black holes (IMBHs) have also been proposed, where different candidates have been

identified as summarized by (Greene et al., 2020), but none have been confirmed and from both theoretical and observational perspectives, gravitational runaway is unlikely to take off in typical globular clusters, though the most massive star clusters may still host such events.

Finally, interesting works have been carried out that can be read for more detail in (Kashlinsky, 2021) about cosmological advection flows in the presence of primordial black holes as dark matter in the context of the formation of first sources of light.

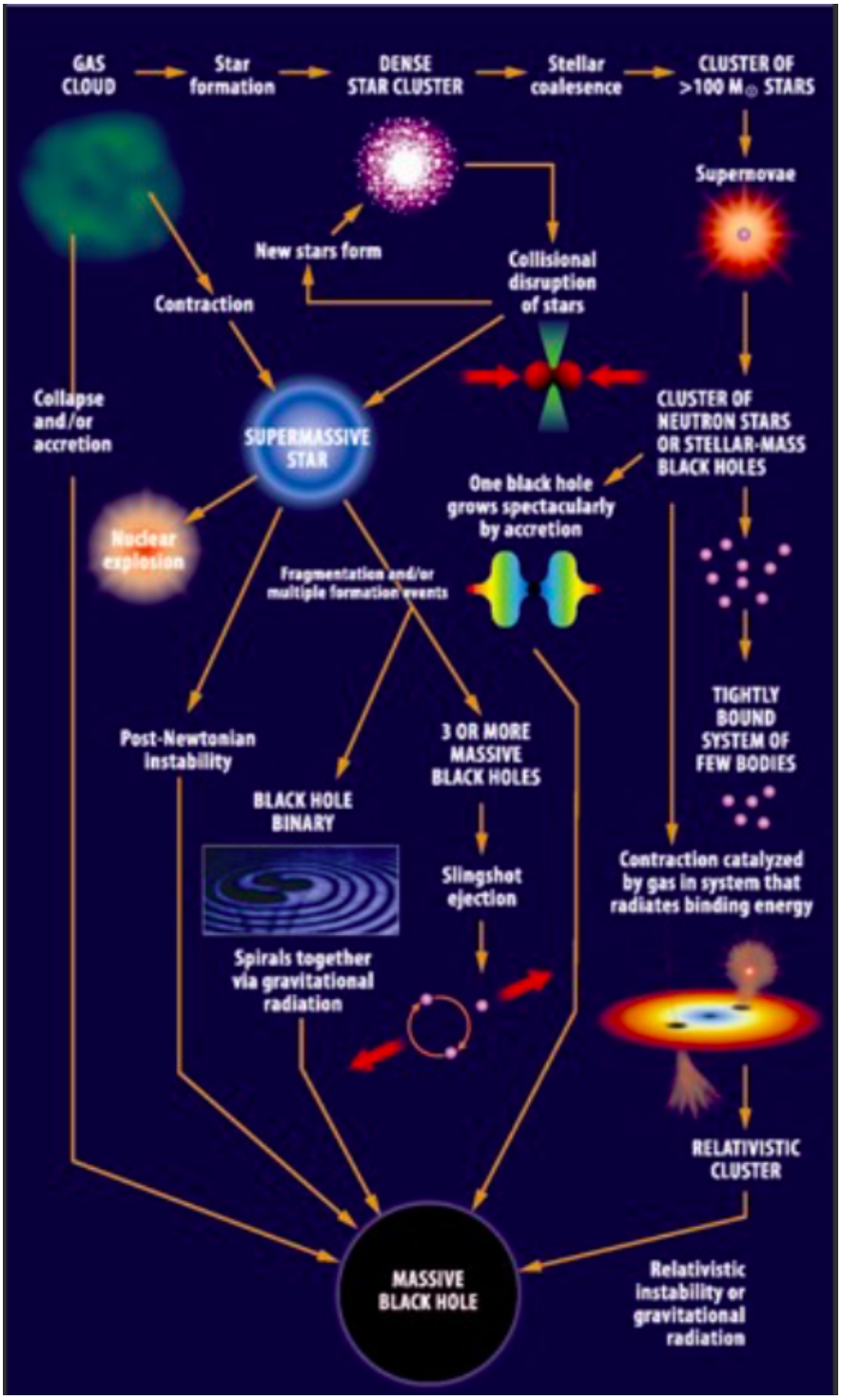

Figure 1.1.2: MBH formation scheme. Source: (Begelman and Rees, 2009).

1.2 Poulation III stars

The objects of this era marked the end of the cosmic dark age and the first stars in the universe arose a few hundred million years after the Big Bang, leading to a fundamental transformation of the early Universe and the initial enrichment with heavy chemical elements. In the early Universe, the primordial gas from which the first stars formed was composed mainly of hydrogen, helium, and metal-free. It is still not known exactly how these stars were formed and the real values of the physical characteristics of these stars since we cannot see them directly because they are too faint to be directly detectable at high redshift, that is why we can only study them through numerical methods in simulations with supercomputers. The temperature of the gas at that time was very high because the cooling was less efficient than in the present-day Universe which has more metals and dust. It has been studied the generic spectral signature of an early population of massive stars at high redshifts from which it has been obtained that for metal-free stars the generic spectrum resembles a black body with an effective temperature of 10^5 K, making these stars highly efficient at ionizing hydrogen and helium (Bromm et al., 2001). Supermassive Population III stars $\gtrapprox 10^4\ M_\odot$ have also been studied to explain the formation of the first quasars (Haemmerlé et al., 2018). A large number of scientists agree that the mass of these stars varies between 10 $M_\odot$ and 100 $M_\odot$. Since these stars are massive they live less than stars like the sun. Variations of the initial mass function and also a universal mass function for these stars have been studied by (Kroupa, 2001). The first stars are thought to be one of the dominant sources of hydrogen reionization in the early Universe, with their high luminosities and surface temperatures expected to drive high ionizing photon production rates (Murphy et al., 2021). Because they are poor in metals these production rates are higher (Schaerer, 2002).

Theoretical studies have been done with the use of the Λ Cold Dark Matter (ΛCDM) model, which explains the observations of the cosmological structure since it provides the initial conditions for the primordial star formation (Bromm, 2013a).

From this time to the present the universe has expanded rapidly and has also cooled. Studies that include the effect of gas cooling via molecular hydrogen suggest that the minihalos have a total mass of $\approx 10^6\ M_\odot$ and collapsed at redshifts z $\simeq$ 20-30 (Bromm, 2013b). Some of the latest studies that have been

done related to predictions of what the James Webb Space Telescope might observe of these stars see (Windhorst et al., 2018), a satellite that was finally launched a few months ago on December 25, 2021. It is also a prediction that ELT-HARMONI will be able to observe population III stars (Grisdale et al., 2021).
Population III stars were called the stars of the early universe that formed from the primordial gas, being these very massive and with zero metallicity. Since these stars are at high redshift, they are too weak to be studied observationally. This is why what we know is based on theoretical studies accompanied by simulations. At first, it was thought that this could have been a not-so-complicated process since the environment was mostly composed of hydrogen and helium, but today we know that this process is as complicated as the current star formation process. Now we know that the accretion disks that build up around the first stars are highly susceptible to fragmentation. So it has been proposed that Population III stars are binaries or members of multiple stellar systems and clusters. It is estimated that the masses of these stars are very wide. The masses have a relatively flat distribution that spans the substellar regime up to several hundred solar masses, with the most likely values being around a few tens of solar masses (Klessen, 2019). In current numerical simulations of the star formation process, more knowledge is lacking about the effect of higher resolution in the simulations, a larger fraction of the star formation timescales, including important physical processes like the protostellar feedback, magnetic fields, heating from dark matter annihilation, WIMP dark matter, cosmic rays, relative streaming velocity between baryons and dark matter in the center of a halo or a three-dimensional approach to understanding more about the gas fragmentation or the dynamical impact of stellar radiation on the infalling gas. Therefore there is still a large computational gap to resolve to understand the star formation process.
This area of study is relatively new since it has only been possible to study it with the development of new numerical methods and very powerful supercomputers. There are still no simulations that include all the physical processes involved in a single simulation since it is very complex.
At that time, H_2 was formed more efficiently as

$$H + e^- \rightarrow \gamma + H^-$$

$$H^- + H \rightarrow H_2 + e^-$$

(the H^- channel) via gas-phase reactions in a cloud of primordial composition. Future missions such as Transient High-Energy Sky and Early Universe Surveyor (THESEUS), a space telescope that will observe Population III stars, will help to understand among other physical processes the life cycle of the first stars and thus the cosmic history of star formation (Tanvir et al., 2021).

1.3 Nuclear star clusters

Nuclear star clusters (NSCs) are dense and massive assemblies of stars found at the centers of most galaxies. Many properties of NSCs vary with the properties of their host galaxies. It has also been studied that a clear transition occurs in galaxies with a mass of $\approx 10^9\ M_\odot$ where the characteristics of nuclear star clusters change. The latest work on the formation of star clusters shows that atomic-cooling halos in which the star clusters form are affected by dark matter motions which reduce the stellar tidal disruption events rates (Sakurai et al., 2019). A possible route of black hole seed formation has been explored that appeals to a model by Davies, Miller & Bellovary who considered the case of the dynamical collapse of a dense nuclear cluster of stellar black holes subjected to an inflow of gas at the center of pregalactic discs forming at very high redshift. They found that this route is feasible, the formation peaks at redshifts z $\lessapprox$ 10 and occur in concomitance with the formation of seeds from other channels. The channel is competitive relative to others and is independent of the metal content of the parent cluster. This mechanism of gas-driven core collapse requires inflows with masses at least 10 times larger than the mass of the parent star cluster, occurring on time scales shorter than the evaporation/ejection time of the stellar black holes from the core. In this respect, the results provide an upper limit to the frequency of this process (Lupi et al., 2014). Figure 1.3.1 and figure 1.3.2 show a schematic of the formation of nuclear star clusters and black hole seeds from these nuclear star clusters.

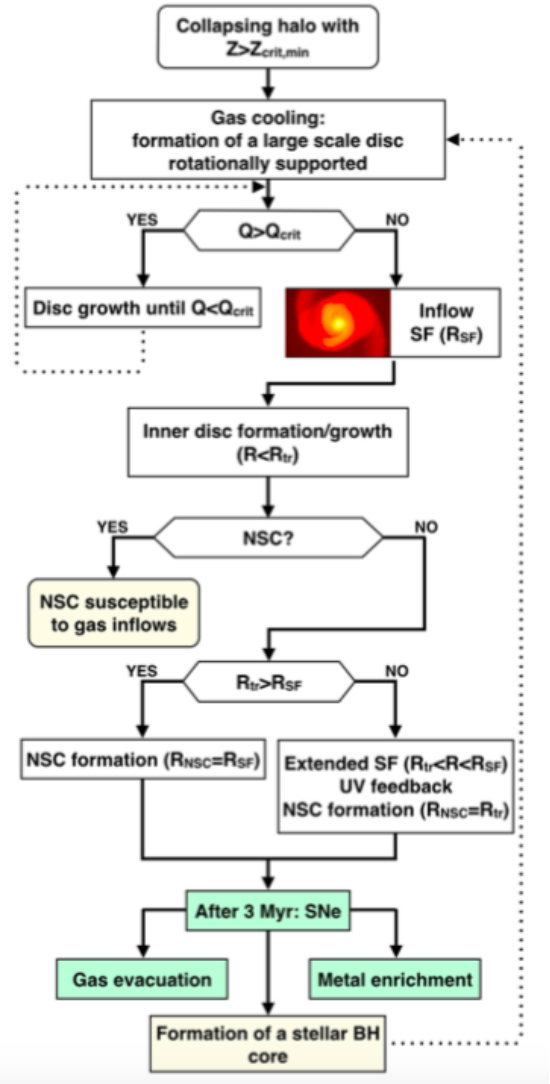

Figure 1.3.1: Flow chart of an isolated halo with Z > Z_{crit}, starting from gas cooling until the formation of an NSC in the center of the halo. Source: (Lupi et al., 2014).

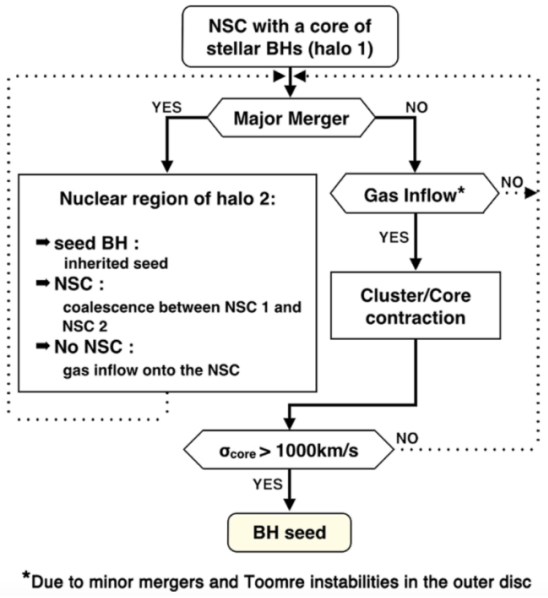

Figure 1.3.2: Flow chart reporting the NSC contraction process leading to the formation of a single seed BH from the merger among stellar mass black holes. Source: (Lupi et al., 2014).

Other important references are (Regan and Haehnelt, 2009) who studied pathways to form massive black holes and compact star clusters in pre-galactic dark matter haloes with virial temperatures $\gtrapprox 10\ 000\ K$ where black holes form at the centers via a stellar seed black hole, a quasistar or via a nuclear star cluster in dark matter (DM) haloes. The latest studies of runaway collisions in dense clusters that may lead to the formation of supermassive black hole (SMBH) seeds found that mass loss can significantly affect the final mass of the possible SMBH seed. Considering a constant mass loss of 5 % for every collision, it can lose between 60-80 % of the total mass that is obtained if the mass loss were not considered. Using instead analytical prescriptions for the mass loss, the mass of the final object is reduced by 15-40 %, depending on the accretion model for the cluster that is studied (Alister Seguel et al., 2020). It has also been studied how supermassive stars (SMSs) with masses $\approx 10^3 - 10^5\ M_\odot$ could be formed via gas accretion and runaway stellar collisions in high-redshift, metal-poor nuclear star clusters (NSCs) and after the formation of SMBHs through the collapse of supermassive stars (SMSs) into seed black holes which could grow up to the SMBHs with a few times $10^9\ M_\odot$ observed at z $\approx$ 7. These are highly sensitive to the initial conditions and the assumed recipe for the accretion, due to the highly chaotic nature of the problem (Das et al., 2021).

Another topic of investigation is the interplay among stellar dynamics, gas accretion, and protostellar evolution. Gas accretion onto the protostars enhances their radii, resulting in an enhanced collisional cross-section. The fraction of collisions can increase from 0.1 to 1 % of the initial population to about 10 % when compared to gas-free models or models of protostellar clusters in the local Universe. This way very massive objects can form despite initial fragmentation, making the first massive protostellar clusters viable candidate birthplaces for observed supermassive black holes (Boekholt et al., 2018). For clusters with a moderate initial central concentration and a realistic IMF, the ratio of core-collapse time to initial half-mass relaxation time is typical ≈ 0.1, in agreement with the value previously found by direct N-body simulations for much smaller systems. Remarkably, for all realistic initial conditions, the mass of the collapsing core is always close to $\approx 10^{-3}$ of the total cluster mass, very similar to the observed correlation between the central black hole mass and the total cluster mass in a variety of environments (Gurkan et al., 2004).

1.4 Previous work on clusters and collisions of Population III stars

One of the latest works that have been pursued is that of (Reinoso et al., 2018) who concluded that collisions in massive Pop. III clusters were likely relevant to form the first intermediate-mass black holes, particularly in more massive Pop. III clusters as expected in the first atomic cooling halos. They derived a more significant enhancement by a factor of 15 and 32 for such massive systems.
On the other hand, it has been found by (Reinoso et al., 2020), who included a background potential and compared to the results of simulations with no background potential with simulations that did have a background potential, that the background potential increases the velocities of the stars, causing an overall delay in the evolution of the clusters and the runaway growth of a massive star at the center. In this case, the population of binary stars is lower due to the increased kinetic energy of the stars, initially reducing the number of stellar collisions, and the relaxation processes are also affected. On the other hand, the external potential enhances the mass of the merger product by a factor ≈ 2 if the collisions are maintained for a long time.

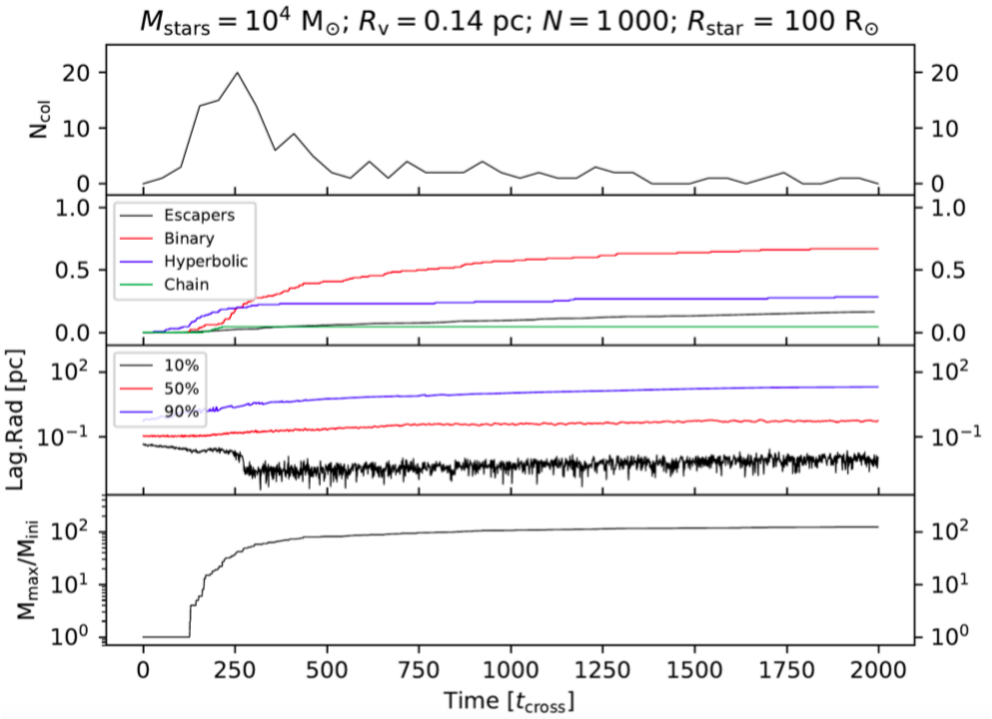

Figure 1.4.1: Evolution of a cluster with $N = 1000$ stars, total mass $M_{\rm stars} = 10^4\ M_\odot$, $R_{\rm v} = 0.14$ pc, and $R_{\rm star} = 100\ R_\odot$. Source: (Reinoso et al., 2020).

In figures 1.4.1 and 1.4.2 the uppermost panel shows the number of mergers as a function of time. The second panel shows the fraction of binaries, hyperbolics (which are stars that are not gravitationally bound), chains (which occur between stars that are part of a higher-order system), and the stars that escape from the cluster as a function of time. The third panel shows the 10 %, 50 %, and 90 % Lagrangian radii as a function of time. And the final panel shows the mass growth of the most massive object in the cluster divided by the initial mass of the stars as a function of time.

Here we can see how the collisions occur afterward when we simulate the effects of the gas with an external potential. The number of stars that escape from the cluster is much smaller in the presence of an external potential, the central part of the cluster that we can see if we enclose 10% of the mass of the cluster collapses while the outermost parts expand and finally with an external potential the mass of the central object becomes larger in time.

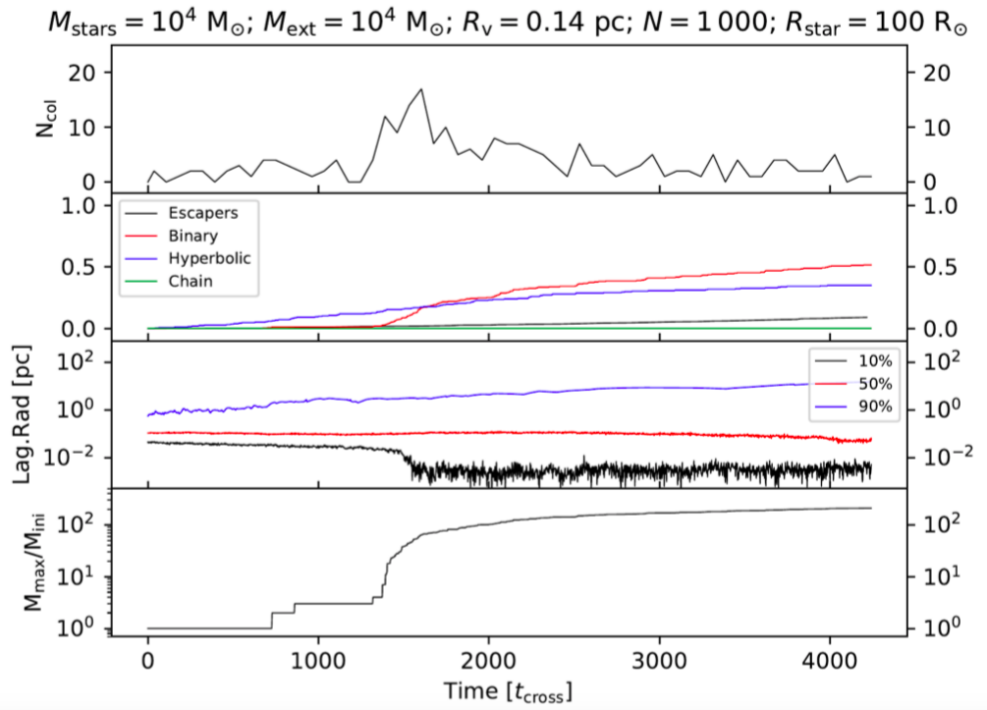

Figure 1.4.2: Evolution of a cluster with $N = 1000$ stars, total mass $M_{\rm stars} = 10^4$ M$_\odot$, $R_{\rm v} = 0.14$ pc, and $R_{\rm star} = 100$ $R_\odot$ and in the center of the cluster an external potential with $M_{\rm ext} = 10^4$ $M_\odot$. Source: (Reinoso et al., 2020).

1.5 Comparison with theoretical expectations for nuclear clusters at galaxy centers

In the paper (Escala, 2021) the author proposes a new formation scenario for massive black hole formation driven by stellar collisions in galactic nuclei in which massive black holes and nuclear stellar clusters are different evolutionary paths of a common formation mechanism.

The collision time scale for any virialized stellar system is defined by

$$t_{\rm coll} = \frac{1}{n\Sigma_0}\sqrt{\frac{R}{GM}}, \tag{1.5.1}$$

where n is the number density, Σ_0 is the effective cross section, R is the characteristic radius of the system, G is the gravitational constant and M is the total mass of the cluster.

If the age of the universe, $t_{\rm H}$, is comparable or longer than the collision time $t_{\rm coll}$

$\leq t_{\rm H}$, it is equivalent to the following condition

$$\left(\frac{4\eta}{300R_{\odot}^{2}t_{\rm H}G^{1/2}}\right)^{2/3} \leq MR^{-7/3}, \tag{1.5.2}$$

where η is the mass of the stars normalized by $M_{\odot}$. And the other constants $M_{\odot}$, $R_{\odot}$, $t_{\rm H}$ and G are the solar mass, the solar radius, the age of the universe and the gravitational constant, respectively.
If we consider that a virialized system has a radius R equal to $R = GM/\sigma^2$, equation 1.5.2 can be written as

$$\sqrt{\frac{4\eta}{300\sigma_{\odot}t_{\rm H}}} \leq \frac{\eta}{M}\left(\frac{\sigma}{\sigma_{\odot}}\right)^{3.5}, \tag{1.5.3}$$

where σ is the characteristic dispersion velocity of the system and $\sigma_{\odot}$ is the solar characteristic dispersion velocity of the system.
If the age of the universe, $t_{\rm H}$, is comparable or longer than the relaxation time $t_{\rm relax} \leq t_{\rm H}$, it is equivalent to the following condition

$$R \leq \left(\frac{t_{\rm H}\eta}{0.1}\ln\left(\frac{M}{\eta}\right)\right)^{2/3}\left(\frac{G}{M}\right)^{1/3}, \tag{1.5.4}$$

where

$$N = M/\eta. \tag{1.5.5}$$

Figure 1.5.1 shows the nuclear stellar clusters as red circles, the well-resolved MBHs as black circles, and the unresolved MBHs as white circles. The black star is M87's black hole shadow. The black line denotes the positions of the Schwarzschild radius as a function of mass. The solid blue line represents the condition given by equation 1.5.2 for $t_{\rm H} = 10^{10}$ years ($\hat{\rho}_{\rm crit} \approx 10^{7}\ M_{\odot}\ pc^{-7/3}$ for solar mass stars, $\eta = 1$). The horizontal green line represents the condition given by equation 1.5.3 ($\approx 3.5 \times 10^{8}\ M_{\odot}$). The dashed green line denotes the condition given by equation 1.5.4 for $t_{\rm H} = 10^{10}$ years, which intersects with the solid blue line at the same critical mass determined by equation 1.5.3. The positions of NSCs are restricted within the boundaries defined by the collisional stable region for NSCs, denoted by the thick blue and green lines. It also explains that NSCs will be unstable for masses larger than 10^{8} M which would explain the absence of NSCs with these masses.

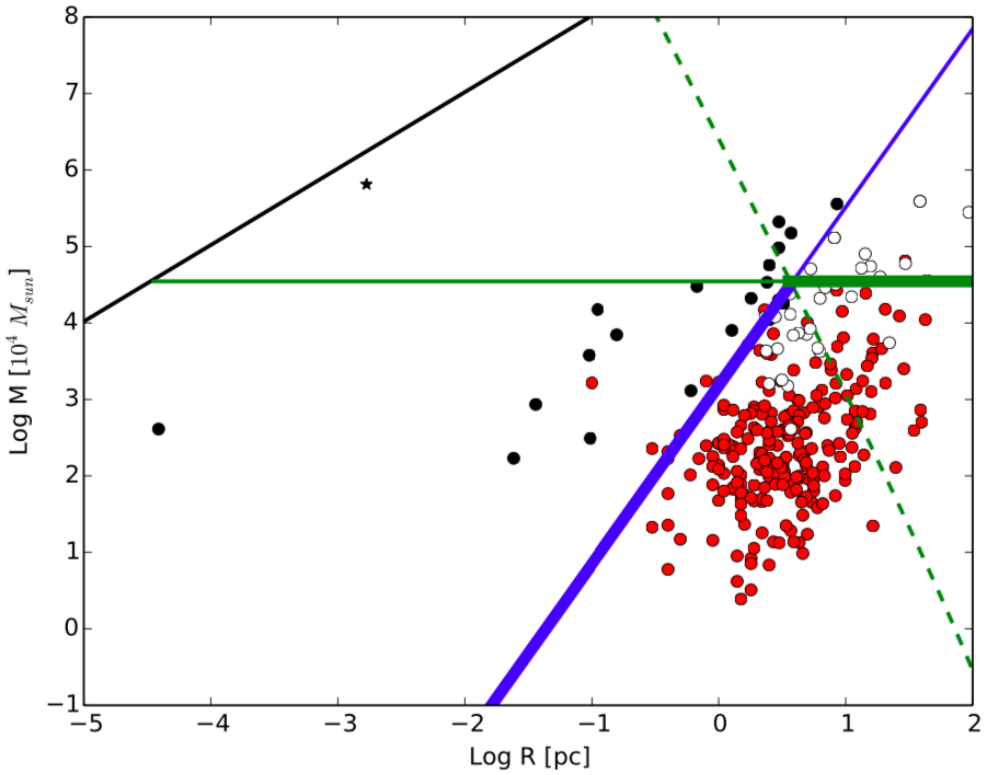

Figure 1.5.1: Measured masses versus effective radius diagram. From: (Escala, 2021).

Figure 1.5.2 shows the observed black hole formation efficiency $\epsilon_{\rm BH} = (1+\frac{M_{\rm NSC}}{M_{\rm BH}})^{-1}$ or what is the same $\epsilon_{\rm BH} = M_{\rm BH}/M_{\rm CMO}$ as a function of the total mass in the central massive object $M_{\rm CMO} = M_{\rm NSC} + M_{\rm BH}$, with both quantities computed using the MBHs and NSCs masses from the dataset by (Neumayer et al., 2020), represented by black circles. The efficiency has two dominant values for black hole efficiencies ($\epsilon_{\rm BH} \leq 0.15$ at $M_{\rm CMO} \leq 3 \cdot 10^7\ M_\odot$ and $\epsilon_{\rm BH} \geq 0.9$ for $M_{\rm CMO} \geq 3 \cdot 10^8\ M_\odot$) and a transition close to a step function of the mass. Upper limits for the efficiencies $\epsilon_{\rm BH}$ are denoted by lower triangles, while lower limits for $\epsilon_{\rm BH}$ by upper triangles, displaying the same trend of the black circles but with larger scatter at lower CMO masses.

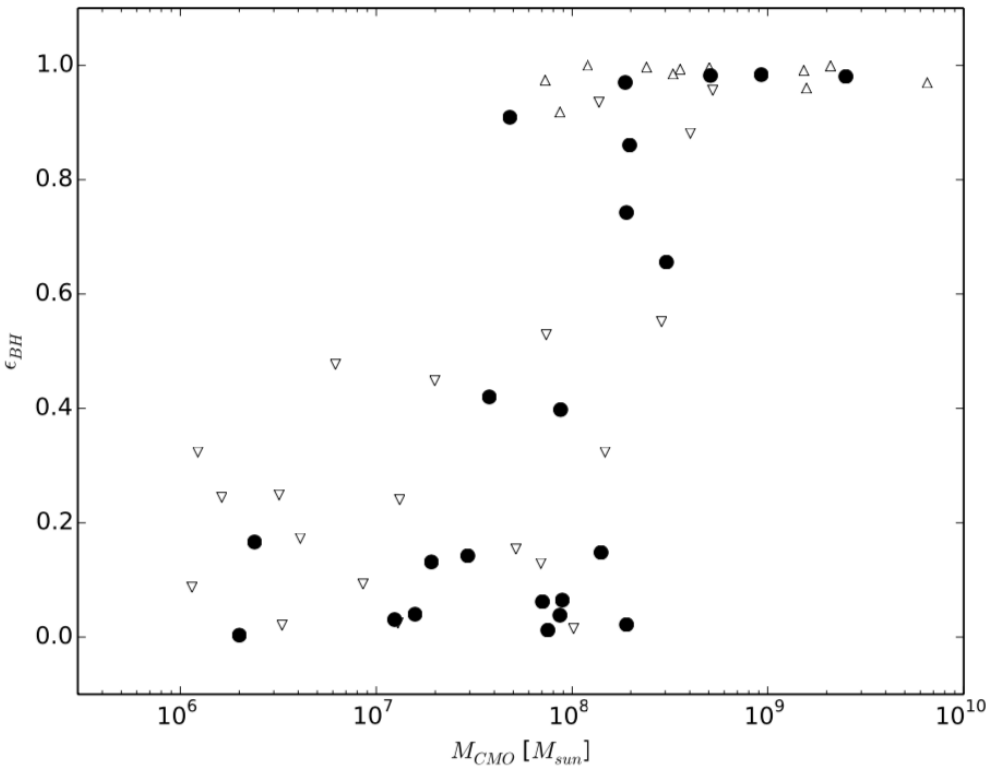

Figure 1.5.2: Mass of the CMO versus the observed efficiency of the black holes formation diagram. Source: (Escala, 2021).

Figure 1.5.3 shows the collision and relaxation timescales in the mass versus radius diagram for clusters composed of solar mass stars ($\eta = 1$), for different cluster ages $t_{\rm H}$: 10^{10} yr in blue, 10^8 yr in green and 10^6 yr in purple. For each color with a different $t_{\rm H}$, clusters on the left side of the solid curves fulfill the condition $t_{\rm coll} \leq t_{\rm H}$ or $t_{\rm relax} \leq t_{\rm H}$, with the intersection of solid curves dividing the stable $t_{\rm relax} \leq t_{\rm coll}$ and the unstable $t_{\rm coll} \leq t_{\rm relax}$ regions. The yellow line denotes the same conditions for 100 $M_\odot$ Pop III stars with $t_{\rm H} = 10^6$ yr. The dotted black line denotes the condition $t_{\rm relax} = t_{\rm coll}$ for clusters composed of solar mass stars ($\eta = 1$) and the dotted red, for clusters of more massive Pop III stars ($\eta = 100$). The collision times of the NSCs measured today can be assumed to be longer than they were at the formation.

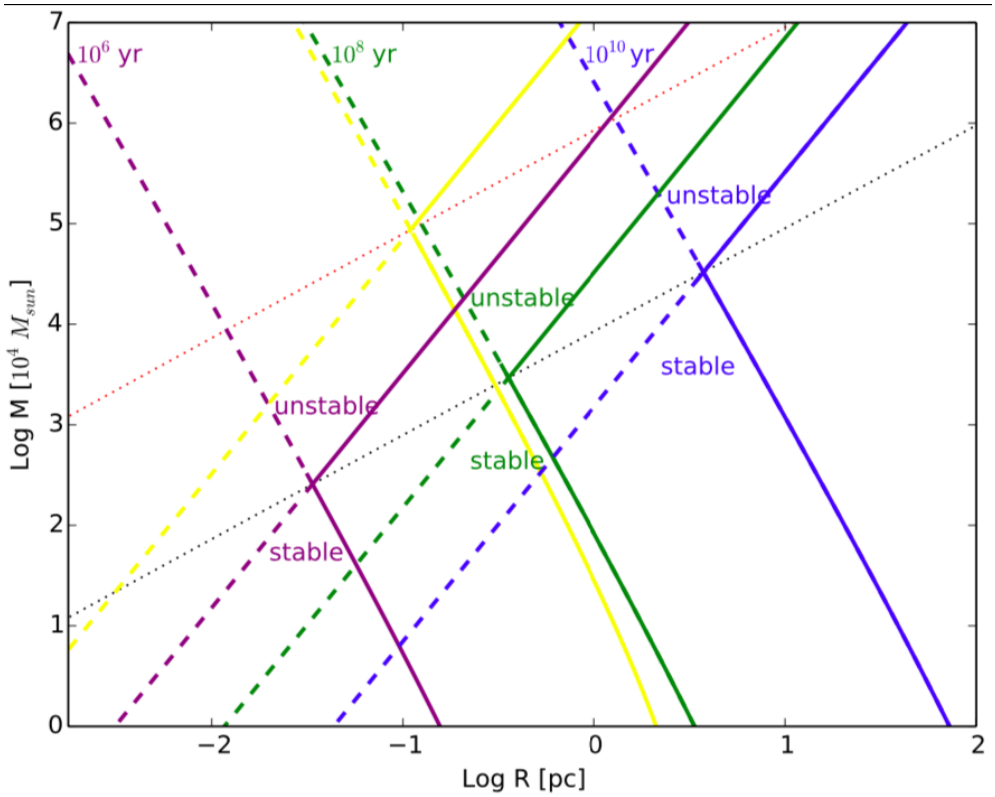

Figure 1.5.3: Collision and relaxation timescales in the mass versus radius diagram. Source: (Escala, 2021).

Chapter 2

Methodology

2.1 NBODY6++

To perform the simulations of this thesis we used the NBODY6++ GPU code, designed to speed up N-body simulations of large numbers of particles (Wang et al., 2015).

The code NBODY6++ GPU directly integrates Newton's equations of motion for many bodies very precisely, giving us information on the dynamic evolution of star clusters. It is used to simulate systems that collide with high precision and a long integration time. This code has four main characteristics: it is based on a fourth-order prediction–correction method (Hermite scheme), individual and block time–steps, a neighbor scheme (Ahmad–Cohen scheme), a regularization scheme for close encounters (KS-Regularization), and few-body subsystems which are described in the manual for the computer code written by (Khalisi et al., 2019). For further discussion of previous versions of the NBODY code see (Aarseth, 1999, 2001).

2.1.1 Hermite scheme

Each particle is determined by its velocity $\mathbf{v_0}$, mass m and position $\mathbf{r_0}$ at time t_0. The acceleration equation and its time derivative due to all the other particles are given for a particle i by

$$\mathbf{a}_{0,\mathrm{i}} = -\sum_{\mathrm{i}\neq\mathrm{j}} Gm_{\mathrm{j}} \frac{\mathbf{R}}{R^3}, \tag{2.1.1}$$

$$\dot{\mathbf{a}}_{0,\mathrm{i}} = -\sum_{\mathrm{i}\neq\mathrm{j}} Gm_{\mathrm{j}} \left[\frac{\mathbf{V}}{R^3} + \frac{3\mathbf{R}(\mathbf{V}\cdot\mathbf{R})}{R^5} \right], \tag{2.1.2}$$

where G is the gravitational constant; $\mathbf{R} = \mathbf{r}_{0,\mathrm{i}} - \mathbf{r}_{0,\mathrm{j}}$ is the relative coordinate; R=$|\mathbf{r}_{0,\mathrm{i}} - \mathbf{r}_{0,\mathrm{j}}|$ the modulus; and $\mathbf{V} = \mathbf{v}_{0,\mathrm{i}} - \mathbf{v}_{0,\mathrm{j}}$ the relative space velocity to the particle j.

The Hermite scheme follows the trajectory of the particle by first predicting a new position and velocity for the next time step t using the Taylor series for $\mathbf{r}_{\mathrm{i}}(t)$ and $\mathbf{v}_{\mathrm{i}}(t)$ given by

$$\mathbf{r}_{\mathrm{p,i}}(t) = \mathbf{r}_0 + \mathbf{v}_0(t-t_0) + \mathbf{a}_{0,\mathrm{i}}\frac{(t-t_0)^2}{2} + \dot{\mathbf{a}}_{0,\mathrm{i}}\frac{(t-t_0)^3}{6}, \tag{2.1.3}$$

$$\mathbf{v}_{\mathrm{p,i}}(t) = \mathbf{v}_0 + \mathbf{a}_{0,\mathrm{i}}(t-t_0) + \dot{\mathbf{a}}_{0,\mathrm{i}}\frac{(t-t_0)^2}{2}. \tag{2.1.4}$$

(But so far the requirements for an accurate high-order integrator are still missing.) Then, an improvement is made using Hermite interpolation which approximates the higher accelerating terms by another Taylor series:

$$\mathbf{a}_{\mathrm{i}}(t) = \mathbf{a}_{0,\mathrm{i}} + \dot{\mathbf{a}}_{0,\mathrm{i}}\cdot(t-t_0) + \frac{1}{2}\mathbf{a}^{(2)}_{0,\mathrm{i}}\cdot(t-t_0)^2 + \frac{1}{6}\mathbf{a}^{(3)}_{0,\mathrm{i}}\cdot(t-t_0)^3, \tag{2.1.5}$$

$$\dot{\mathbf{a}}_{\mathrm{i}}(t) = \dot{\mathbf{a}}_{0,\mathrm{i}} + \mathbf{a}^{(2)}_{0,\mathrm{i}}\cdot(t-t_0) + \frac{1}{2}\mathbf{a}^{(3)}_{0,\mathrm{i}}\cdot(t-t_0)^2. \tag{2.1.6}$$

From equations 2.1.5 and 2.1.6 we need to know the terms $\mathbf{a}^{(2)}_{0,\mathrm{i}}$ and $\mathbf{a}^{(3)}_{0,\mathrm{i}}$. They can be calculated using $\mathbf{r}_{\mathrm{p}}$ and $\mathbf{v}_{\mathrm{p}}$ following the calculation of the equations 2.1.1 and 2.1.2 and they will be $\mathbf{a}_{\mathrm{p,i}}$ and $\dot{\mathbf{a}}_{\mathrm{p,i}}$ respectively. We replace the values of $\mathbf{a}_{\mathrm{p,i}}$ and $\dot{\mathbf{a}}_{\mathrm{p,i}}$ on the left-hand side of the equation 2.1.5 and 2.1.6, after simplifying we obtain

$$\mathbf{a}^{(3)}_{0,\mathrm{i}} = 12\frac{\mathbf{a}_{0,\mathrm{i}} - \mathbf{a}_{\mathrm{p,i}}}{(t-t_0)^3} + 6\frac{\dot{\mathbf{a}}_{0,\mathrm{i}} + \dot{\mathbf{a}}_{\mathrm{p,i}}}{(t-t_0)^2}, \tag{2.1.7}$$

$$\mathbf{a}^{(2)}_{0,\mathrm{i}} = -6\frac{\mathbf{a}_{0,\mathrm{i}} - \mathbf{a}_{\mathrm{p,i}}}{(t-t_0)^2} - 2\frac{2\dot{\mathbf{a}}_{0,\mathrm{i}} + \dot{\mathbf{a}}_{\mathrm{p,i}}}{(t-t_0)}. \tag{2.1.8}$$

Finally, to have a 'corrected' position $\mathbf{r}_{1,\mathrm{i}}$ and velocity $\mathbf{v}_{1,\mathrm{i}}$ of the particle i at the computation time t_1 we need to extend the Taylor series for $\mathbf{r}_{\mathrm{i}}(t)$ and $\mathbf{v}_{\mathrm{i}}(t)$ from equations 2.1.3 and 2.1.4 by two more orders

$$\mathbf{r}_{1,\mathrm{i}}(t) = \mathbf{r}_{\mathrm{p,i}}(t) + \mathbf{a}^{(2)}_{0,\mathrm{i}}\frac{(t-t_0)^4}{24} + \mathbf{a}^{3}_{0,\mathrm{i}}\frac{(t-t_0)^5}{120}, \tag{2.1.9}$$

$$\mathbf{v}_{1,\mathrm{i}}(t) = \mathbf{v}_{\mathrm{p,i}}(t) + \mathbf{a}^{2}_{0,\mathrm{i}}\frac{(t-t_0)^3}{6} + \mathbf{a}^{(3)}_{0,\mathrm{i}}\frac{(t-t_0)^4}{24}. \tag{2.1.10}$$

This way we obtain the Hermite scheme able to obtain high-order accelerations from the combination of low-order terms with only the first derivative of the equations.

The local error in $\mathbf{r}$ and $\mathbf{v}$ within the two-time steps $\Delta = t_1 - t_0$ is expected to be of order $\vartheta(\Delta t^5)$, and the global error for a fixed physical integrator time scales with $\vartheta(\Delta t^4)$ (Makino, 1991).

2.1.2 Individual and block time steps

So far we understand that stellar systems have a huge dynamical range in radial and temporal scales with time scales from periods of some days for binaries to relaxation times of star clusters of billions of years. There typically is a large dynamic range in the average local stellar density from the center to the very outskirts of clusters, where it dissolves into the galactic tidal field. If we consider the timestep required for the two closest bodies they would determine the time-step of the force calculation for the whole rest of the system. Then, if we choose a small time step the evolution of the system will be very time-consuming which would not allow us to evolve the simulation for a long enough time. And if we choose a larger time step close encounters will not be calculated correctly. So the idea here is to mix both the small time steps and the larger time steps for the whole system; therefore for large changes, the force is calculated via small time steps, and for small changes, the force is applied on larger time steps.

First, the individual time-step scheme (Aarseth, 1963) was studied, and then the block time-steps.

Each particle in NBODY6++ GPU is assigned its own Δt_{i} like in the block time steps in figure 2.1.1. The particle i has the smallest time step at the beginning of the simulation, so its phase space coordinates are calculated at each time step. The particle k has a time step that is twice the time-step for the particle i, at the odd time steps the full force calculation is just 'predicted' and a full force calculation is due at the dotted lines. The step width may be altered or not after the end of the integration cycle for a particle for example for k and l beyond the label '8'. The time steps have to stay commensurable with both each other as well as the total time, such that the hierarchy is guaranteed. This is what is called a block step scheme.

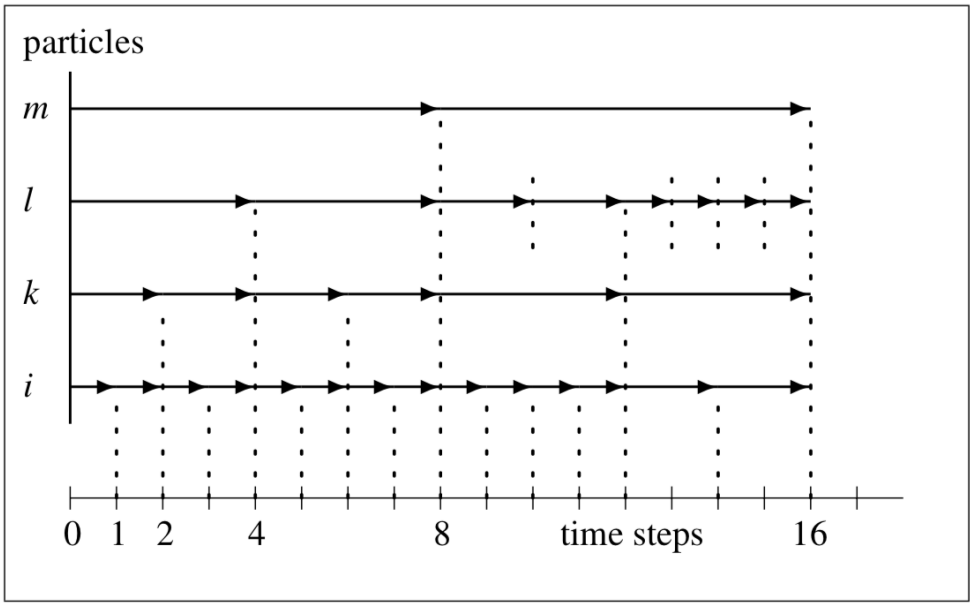

Figure 2.1.1: Illustration of the block time step scheme in NBODY6++ GPU for four particles. Source: NBODY6++ GPU Manual for the computer code (Khalisi et al., 2019). You can find this document here https://github.com/nbodyx/Nbody6ppGPU/tree/master/doc.

A first estimate for the time step could be the rate of change of the acceleration $\Delta t_\mathrm{i} \propto \sqrt{\mathbf{a}_\mathrm{i}/\dot{\mathbf{a}}_\mathrm{i}}$. But it turns out that for special situations in many body systems, it provides some undesired numerical errors. After some experiments, the following formula was adopted (Aarseth, 1985).

$$\Delta t_\mathrm{i} = \sqrt{\eta \frac{|\mathbf{a}_{1,\mathrm{i}}||\mathbf{a}^{(2)}_{1,\mathrm{i}}| + |\dot{\mathbf{a}}_{1,\mathrm{i}}|^2}{|\dot{\mathbf{a}}_{1,\mathrm{i}}||\mathbf{a}^{(3)}_{1,\mathrm{i}}| + |\mathbf{a}^{(2)}_{1,\mathrm{i}}|^2}}, \tag{2.1.11}$$

where η is a dimensionless accuracy parameter that controls the error. In most applications, it is taken to be $\eta \approx 0.01$ to 0.02.
It can be noticed that after some time there will be a grouping of particles (block) due to the movement at each time step.

2.1.3 Ahmad–Cohen scheme

As we consider more particles in the simulations it will take much longer to calculate the full force for each particle within the system. Therefore, it is desirable to use a method to speed up the calculations while retaining the collisional approach.

One way to achieve this is to employ the 'neighbor scheme' suggested by (Ahmad and Cohen, 1973). The idea of the Ahmad-Cohen scheme is to split the force polynomial from equation 2.1.5 on a given particle i into two parts, an irregular and a regular component:

$$\mathbf{a}_{\mathrm{i}} = \mathbf{a}_{\mathrm{i,irr}} + \mathbf{a}_{\mathrm{i,reg}}. \tag{2.1.12}$$

The irregular acceleration $\mathbf{a}_{\mathrm{i,irr}}$ due to the particles in the neighborhood of a certain particle i (in the code, FI and FIDOT are the irregular force and its time derivative at the last irregular step; internally some routines use FIRR and FD as a local variable). As these particles are close, they give rise to a stronger fluctuating gravitational force, then it is calculated more frequently than the regular one of the more distant particles that don't change their relative distance to i so quickly (in the code, FR and FRDOT are the regular force and its time derivative at the last regular step; some routines use as a local variable FREG and FDR). The total calculation in equation 2.1.1 can be replaced by a summation over the nearest particles N_{nb} for $\mathbf{a}_{\mathrm{i,irr}}$ and adding a distant contribution from all the others. This contribution is updated using another Taylor series FRDOT (that is the time derivative at the last regular step) and the time derivative of FR (the regular force at the last regular step) at the last regular force computation.

If a particle is a neighbor or not is determined by its distance. All particles inside a specified 'neighbor sphere' with a radius r_{s} as we can see in figure 2.1.2 (Makino and Aarseth, 1992) are kept in a list, which is modified at the end of each regular time step when a total force calculation is carried out. Particles outside this sphere will be calculated for their irregular force FIRR. Also, approaching particles within a surrounding shell satisfying $\mathbf{R} \cdot \mathbf{V} < 0$ are included. This 'buffer zone' serves to identify fast-approaching particles before they come in too far into the neighbor sphere. The neighbor criterion is determined by the relative forces between the particles, not by their distance.

The filled dots inside the sphere are in the list that is filled in to calculate the total force at the beginning of the simulation. The irregular components are calculated first and then the regular ones. At the same time also the first-time derivative is calculated. From the equations 2.1.5 and 2.1.6 the position and velocity of the particle i are predicted.

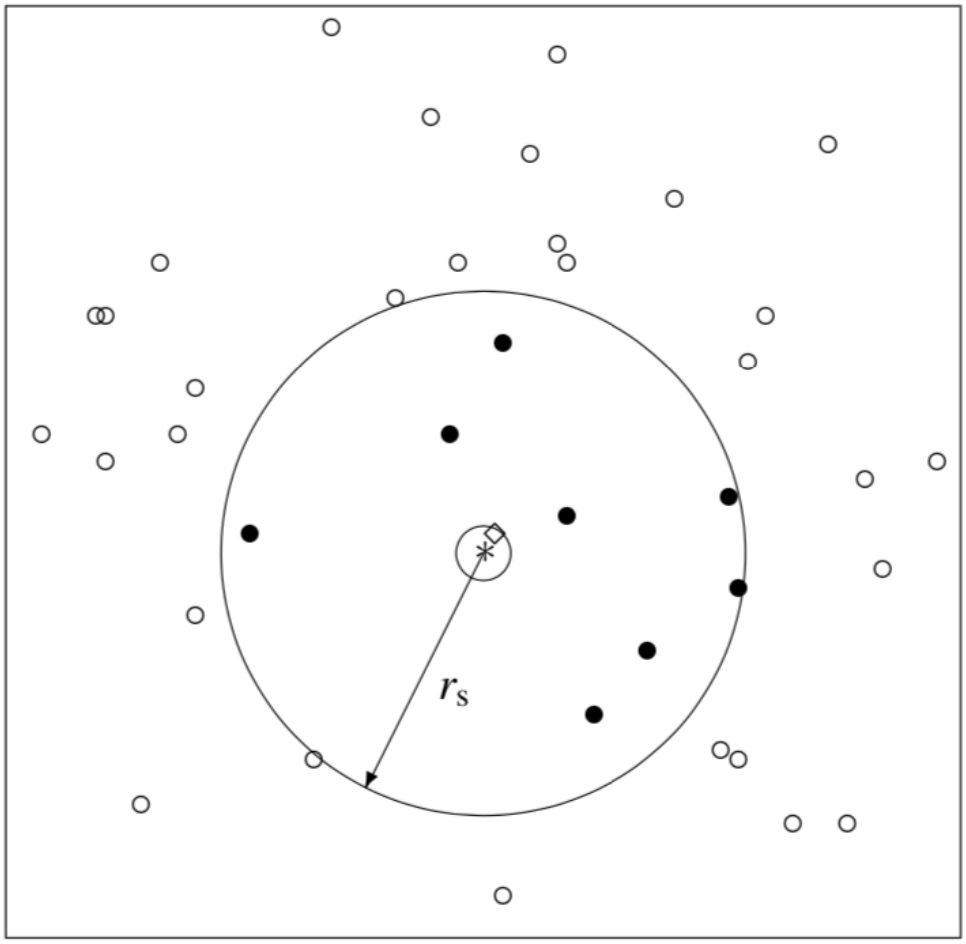

Figure 2.1.2: A neighbor scheme for a particle marked as the asterisk. Source: NBODY6++ GPU Manual for the computer code (Khalisi et al., 2019).

As we can see in figure 2.1.3 at the time $t_{1,\mathrm{irr}}$ the "corrector" is applied only for the irregular acceleration from the neighbors; the regular acceleration is not corrected, but obtained by extrapolating. At the time $t_{2,\mathrm{irr}}$ ocurrs the same. The Hermite predictor-corrector method is also applied and another new list of neighbors is created. Therefore, at certain times only the forces from neighbors (irregular time steps) are calculated, while at other times both the forces from neighbors and distant particles (regular time steps) are calculated.
In the code NBODY6++ GPU the variable NNBOPT controls the size of the neighbor spheres. Its typical values are between 50 and 200 for a very wide range of total particle numbers.
From equation 2.1.11 the accuracy can be tuned by $\eta_{\mathrm{irr}} \approx 0.01$ and $\eta_{\mathrm{reg}} \approx 0.02$ again.

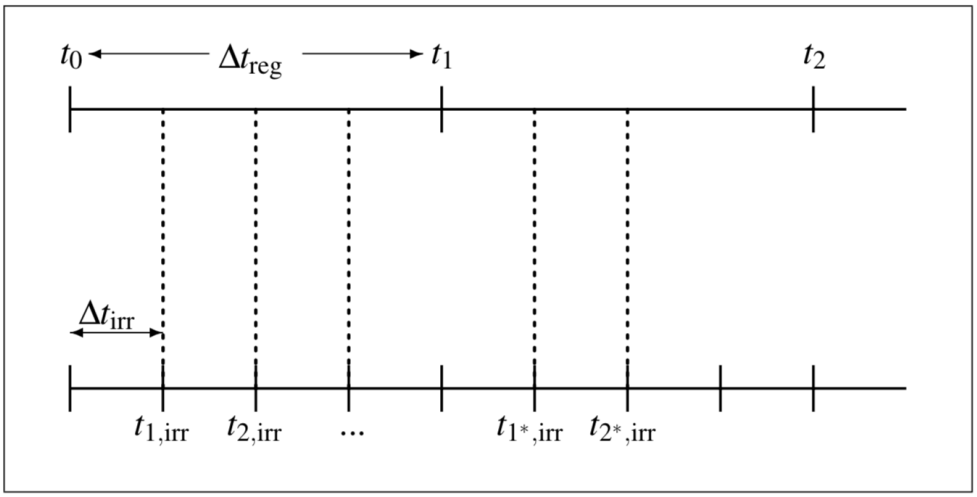

Figure 2.1.3: Illustration of the regular and irregular time steps. Source: NBODY6++ GPU Manual for the computer code (Khalisi et al., 2019).

2.1.4 Regularization of close encounters and few-body subsystems

The small time steps and small distances in the dynamics of close binaries are treated via regularization. This is one of the most expensive calculations within NBODY6++ GPU. The impact parameter determines the close encounters and is smaller than the parameter for a 90-degree deflection,

$$p_{90} = 2G(m_1 + m_2)/v_\infty^2, \tag{2.1.13}$$

where G, m_1, m_2, and v_∞ are the gravitational constant, the masses of the two particles, and their relative velocity at infinity. These close encounters occur more in the center of the cluster since in this place the distances between particles are smaller. What happens is that the relative distances between the particles are very small and their time steps are also very small, which causes the error to grow in these places due to the singularity in the gravitational potentials. This is the problem that regularization resolves. The regularization defines two parameters within NBODY6++ GPU: RMIN and DTMIN. RMIN indicates the maximum separation for a close encounter and when these particles are closer than RMIN (from equation 2.1.13) and the time steps are smaller than DTMIN then the

conditions for regularization are fulfilled. DTMIN is defined as:

$$dt_{\min} = \kappa \left[\frac{\eta}{0.03}\right] \left(\frac{r_{\min}^3}{\langle m \rangle}\right)^{1/2}, \tag{2.1.14}$$

where κ is a free numerical factor, η the general time step factor, and <m> the average stellar mass. That is why regularization is an elegant trick to deal with particles that are as close as the diamond in figure 2.1.2. The principal idea is to take both stars out of the main integration cycle, replace them by their center of mass and advance the usual integration with a composite particle instead of resolving the two components. The two members of the regularized pair (henceforth KS pair) will be relocated to the beginning of all vectors containing particle data, while at the end one additional center of mass (c.m.) particle is created. One of the purposes of the code variable NAME(I) is to identify particles after such a reshuffling of data.

Also, the two particles have to fulfill two more sufficient criteria: that they are approaching each other, and that their mutual force is dominant. In the equations in routine search.f, these sufficient criteria are defined as:

$$\mathbf{R} \cdot \mathbf{V} > 0.1\sqrt{(G(m_1 + m_2)R)}, \tag{2.1.15}$$

$$\gamma := \frac{|\mathbf{a}_{\text{pert}}| \cdot R^2}{G(m_1 + m_2)} < 0.25, \tag{2.1.16}$$

where $\mathbf{a}_{\text{pert}}$ is the vectorial differential force exerted by other perturbing particles onto the two candidates, and R, $\mathbf{R}$, $\mathbf{V}$ are scalar and vectorial distance and relative velocity vector between the two candidates, respectively. The factor 0.1 in the upper equation allows nearly circular orbits to be regularized. The condition $\gamma <$ 0.25 demands that the relative strength of the perturbing forces compared to the pairwise force is one-quarter at most. Then these subsystems are separated from the rest of the system but not unperturbed.

After this, the motion of the new particle is put into a new coordinate system (three-dimensional cartesian space). Any unperturbed two–body orbit in real space is mapped onto a harmonic oscillator in KS–space with double the frequency. The internal time-step of such a KS-regularized pair depends on the parameter ETAU, which is of the order of some 50-100 steps per orbit. The first studies on this topic were done in (Stiefel, 1965). A more modern theoretical version can be found at (Neutsch and Scherer, 1992). The Hamiltonian formalism is explained in

(Mikkola, 1997).

When the perturbation γ falls below a critical value of the input parameter GMIN $\approx 10^{-6}$, it is considered to be unperturbed and the analytical solution for the Keplerian orbit is used instead of doing numerical integration. A little bit misleading is that such unperturbed KS–pairs are denoted in the code as "mergers", e.g. in the number or merges (NM) and the energy of the mergers (EMERGE). Merged pairs can be resolved at any time if the perturbation changes. The two–body KS regularization occurs in the code either for short-lived hyperbolic encounters or for persistent binaries.

In the code, the KS–pair appears as a new particle at the position of the center of mass. The variable NTOT which contains the total number of particles N plus the c.m.'s is increased by 1. When the pair is disrupted, NTOT has decreased again. The maximum number of possible KS– pairs are saved in the variable KMAX, which sets a threshold for the extension of the vector NTOT.

Close encounters between single particles and binary stars are also a central feature of cluster dynamics. Such temporary triple systems often reveal irregular motions, ranging from just a perturbed encounter to a very complex interaction, in which disruption of binaries, exchange of components, and ejection of one star may occur. Although not analytically solvable, the general three–body problem has received much attention. So, the KS–regularization was expanded to the isolated 3– and 4–body problem, and later on to the perturbed 3–, 4–, and finally to the N–body problem. The routines are called triple.f, quad.f, chain.f.

While occurrences of "triple" and "quad" will be rare in a simulation, the chain regularization is invoked if a KS–pair has a close encounter with another single star or another pair. Especially if systems start with a large number of primordial binaries, such encounters may lead to stable (or quasi-stable) hierarchical triples, quadruples, and higher multiples. They have to be treated by using special stability criteria.

A typical way to treat all such special higher subsystems is to define their c.m. to be a pseudo-particle, i.e. a particle with a known sub-structure. The members of the pseudo-particles will be deactivated by setting their mass to zero (ghost particles). At present, there can only be one chain at a time in the code, while merged KS binaries and hierarchical subsystems can be more frequent.

Every subsystem — KS pair, chain or hierarchical subsystem is perturbed. Perturbers are typically those objects that get closer to the object than $R_{\rm sep}$

$= R/\gamma_{\rm min}^{1/3}$, where R is the typical size of the subsystem; for perturbers, the components of the subsystem are resolved in their force computation as well (routines cmfreg.f, cmfirr.f).

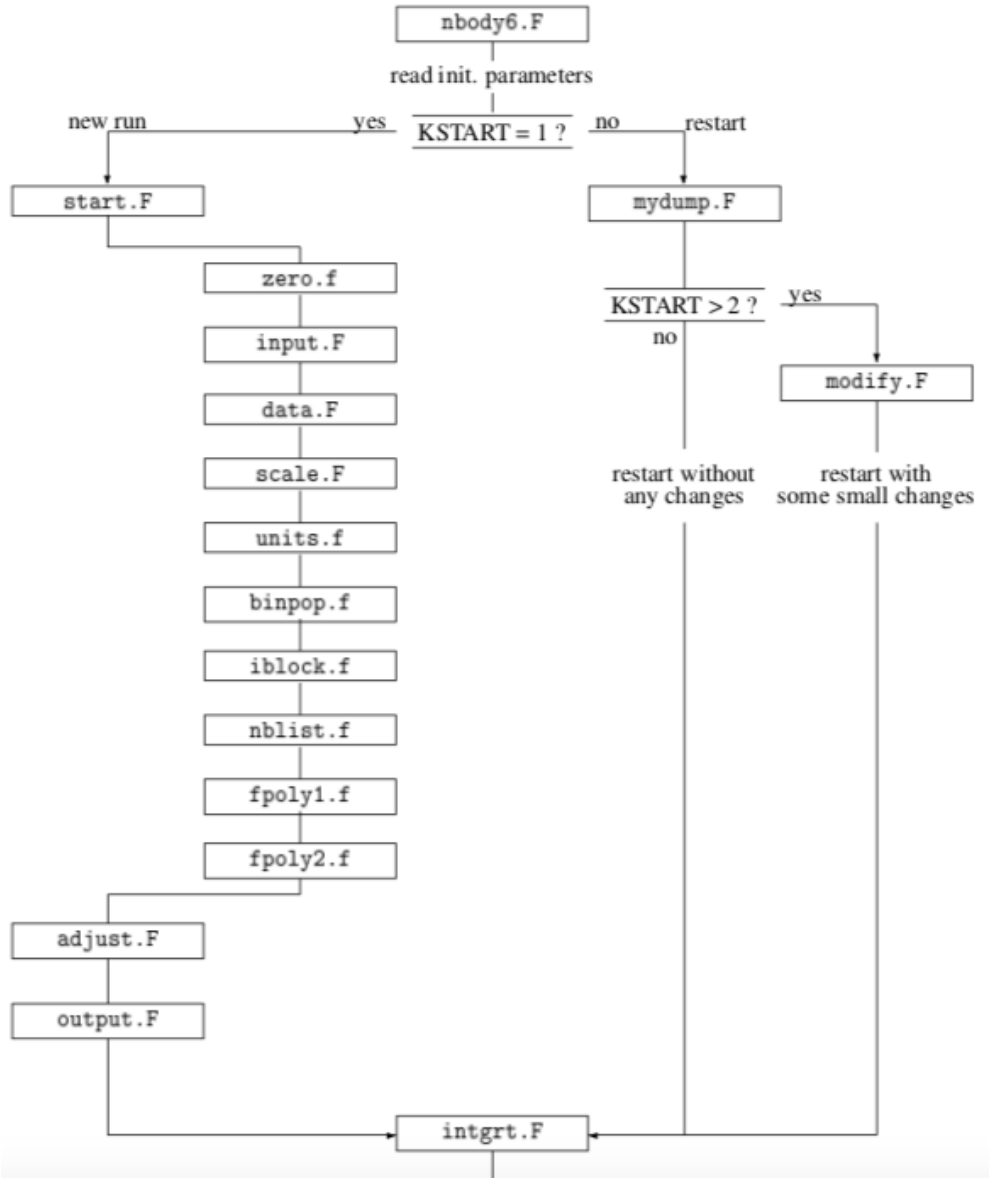

Figure 2.1.4: Flow chart NBODY6++ GPU. Source: NBODY6++ GPU Manual for the computer code (Khalisi et al., 2019).

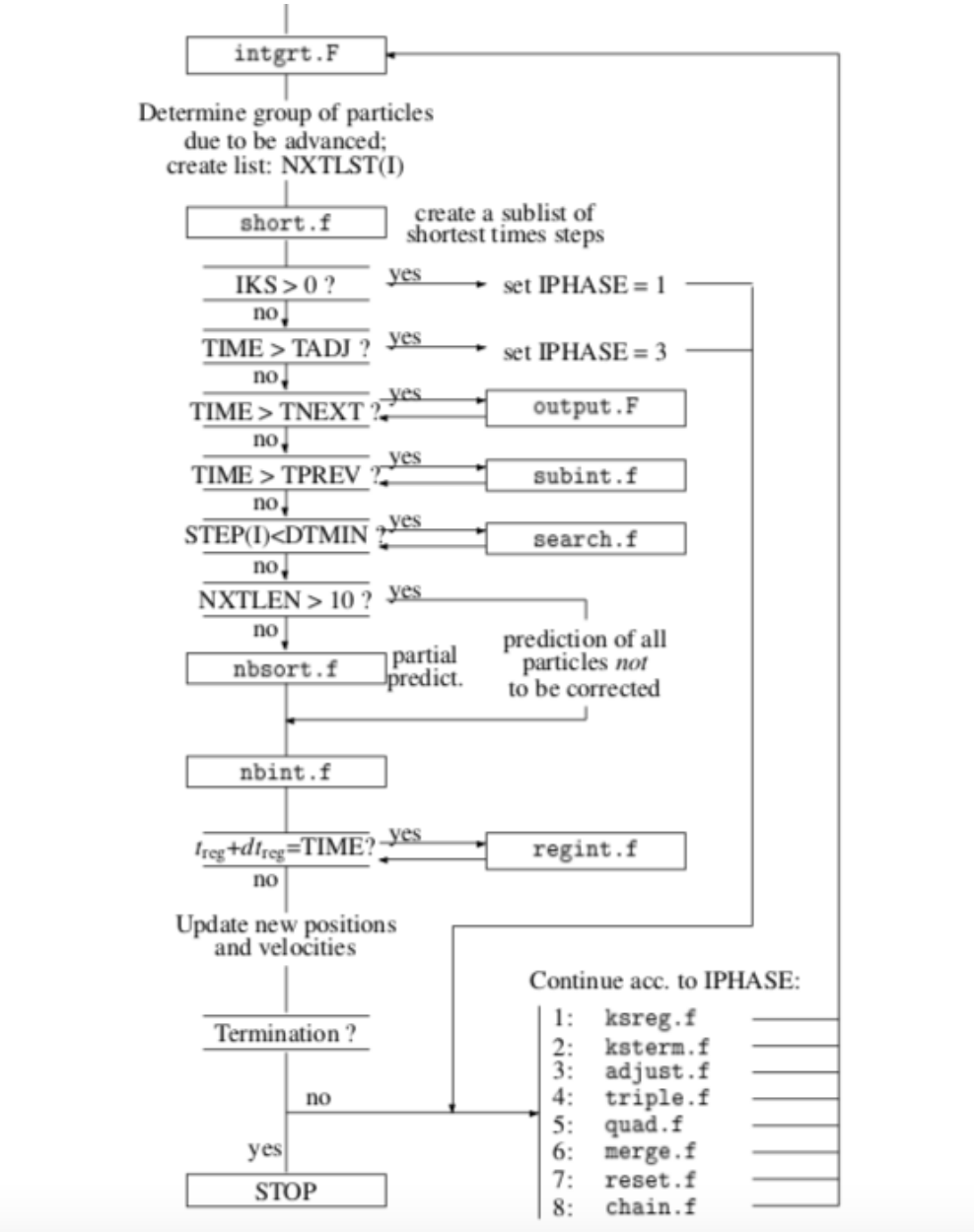

Figure 2.1.5: Flow chart NBODY6++ GPU. Source: NBODY6++ GPU Manual for the computer code (Khalisi et al., 2019).

In the figures 2.1.4 and 2.1.5 we can see the general structure of how the NBODY6++ GPU code works depending on the parameters defined in the input file.

2.2 Description of the numerical setup

2.2.1 Input

We model dense star clusters in virial equilibrium using a Plummer distribution for the stars (Plummer, 1911). Half of our simulations included an analytic background potential, which helps us simulate the effects of the gas within the cluster, which also follows a Plummer density profile.
This is a template of the input file used to carry out the simulations with NBODY6++ GPU. The file was used for all simulations with only minor changes. These small changes are the termination time in N-body units (TCRIT), the virial radius of the cluster (RBAR), the mean mass of the stars (ZMBAR), and the maximum and minimum particle mass (BODY1 and BODYN). The last three parameters have to be the same because we are not considering stellar evolution nor an initial mass function therefore the masses are the same throughout the evolution of the cluster, and the initial radius of the stars in the file instar.F which is in the folder '.../src/Main/'. The NBODY code uses dimensionless units with the name Nbody units. More detail on how these different variables are defined within the code can be found in (Khalisi et al., 2019).
The input file contains more than 90 parameters that must be adjusted for each simulation.
The names of the different input parameters are described below:

Line 1: KSTART, TCOMP, TCRITp, isernb, iserreg, iserks.
Line 2: N, NFIX, NCRIT, NRAND, NNBOPT, NRUN.
Line 3: ETAI, ETAR, RSO, DTADJ, DELTAT, TCRIT, QE, RBAR, ZMBAR.
Line 4: KZ(1), KZ(2), KZ(3), KZ(4), KZ(5), KZ(6), KZ(7), KZ(8), KZ(9), KZ(10).
Line 5: KZ(11), KZ(12), KZ(13), KZ(14), KZ(15), KZ(16), KZ(17), KZ(18), KZ(19), KZ(20).
Line 6: KZ(21), KZ(22), KZ(23), KZ(24), KZ(25), KZ(26), KZ(27), KZ(28), KZ(29), KZ(30).
Line 7: KZ(31), KZ(32), KZ(33), KZ(34), KZ(35), KZ(36), KZ(37), KZ(38), KZ(39), KZ(40).
Line 8: KZ(41), KZ(42), KZ(43), KZ(44), KZ(45), KZ(46), KZ(47), KZ(48),

KZ(49), KZ(50).
Line 9: DTMIN, RMIN, ETAU, ECLOSE, GMIN, GMAX, SMAX.
Line 10: AlPHA, BODY1, BODYN, NBINO, NHIO, ZMET, EPOCHO, DTPLOT.
Line 11: Q, VXROT, VZROT, RTIDE.
Line 12: MP, AP, MPDOT, TDELAY.

Line 1 contains the parameters that are defined in the file nbody6.F. The parameters of lines 2, 3, 4, 5, 6, 7, 8, and 9 are defined in the file input.F. The parameters of line 10 are defined in the file data.F. Scale.F contains the definitions of the parameters of line 11 and finally xtrn10.F includes the definition of the parameters of line 12.
The input file for NBODY6++ GPU is written as follows.
For the case with an external potential:

```
1 1000000.0 1.E6 40 40 0
10000 1 10 43532 190 1 10
0.02 0.01 0.25 1.0 1.0 48000.0 2.0E00 0.05 15.0
0 1 1 0 1 0 4 0 1 2
0 1 0 4 0 0 0 4 3 0
1 1 2 0 0 2 -1 0 0 2
1 0 2 0 0 0 1 1 0 0
0 0 0 0 0 4 -2 0 1 0
1.0E-03 1E-3 0.2 1.0 1.0E-06 0.01 1
1.0 15.0 15.0 0 0 0.0001 0 1.0
0.5 0.0 0.0 0.0
1.0 0.59 10000 10000
```

For the case without an external potential:

```
1 1000000.0 1.E6 40 40 0
10000 1 10 43532 100 1 10
0.02 0.01 0.17 1.0 1.0 24000.0 2.0E00 0.05 15.0
```

0 1 1 0 1 0 4 0 1 2
0 1 0 0 0 0 0 4 3 0
1 1 2 0 0 2 -1 0 0 2
1 0 2 0 0 0 1 1 0 0
0 0 0 0 0 4 -2 0 1 0
1.0E-03 1E-3 0.2 1.0 1.0E-06 0.01 1
1.0 15.0 15.0 0 0 0.0001 0 1.0
0.5 0.0 0.0 0.0

We use a version of the code modified by Bastian Reinoso to include stellar collisions avoiding the use of the stellar evolution routines from the original version. Therefore the mass of the stars is always the same during the evolution of the cluster unless they collide. The simulated cluster has a Plummer distribution. Some simulations include an external analytic Plummer potential. The external analytic Plummer potential can be added on line 5 in column number 4 which corresponds to KZ(14)=4 with an additional line at the end of the input, which is MP that is the total mass of the Plummer sphere in scaled units, AP the Plummer scale factor in N-body units, MPDOT the decay time for gas expulsion and TDELAY the delay time for starting gas expulsion. The evolution of clusters was followed until 10 Myr. The example used is a simulation of 10,000 particles with a Plummer potential until N-body units. Since we don't consider stellar evolution, the stellar mass at the beginning of the simulation and the final stellar mass are the same, i.e. ZMBAR=BODY1=BODYN, which in this case is equal to 15 $M_{\odot}$. The virial radius is 0.05 [pc] and the stellar radius is 1.51 $R_{\odot}$ while the radius of the external potential $R_{\rm v,ext}$ is the same as the virial radius of the stellar distribution.

The crossing time is the time required for a star with a typical velocity to cross the system. The crossing time for a system in virial equilibrium without an external potential is defined by

$$t_{\rm cross} = \sqrt{\frac{R_{\rm v}^3}{GM_{\rm stars}}}, \tag{2.2.1}$$

where $R_{\rm v}$ is the virial radius of the cluster, G is the gravitationsl constant and M is the total mass of the stars.

The relaxation time is the time needed for a system to return to a state of

equilibrium. The half-mass relaxation time for a system with identical particles is defined as

$$t_{\rm rh} = 0.138\frac{N}{ln(\gamma N)}t_{\rm cross} \tag{2.2.2}$$

in the absence of an external potential.
The crossing time including an external potential is defined by

$$t_{\rm cross,ext} = \sqrt{\frac{R_{\rm v}^3}{GM_{\rm stars}}}\frac{1}{1+q}. \tag{2.2.3}$$

The core collapse time scale is related to the crossing time as $t_{\rm cc} \propto (1+q)^4 t_{\rm cross}$. Here q is defined as $q = \frac{M_{\rm ext}}{M_{\rm stars}}$.
Then, the half-mass relaxation time with an external potential can be calculated as

$$t_{\rm rh,ext} = 0.138\frac{N(1+q)^4}{ln(\gamma N)}t_{\rm cross,ext}, \tag{2.2.4}$$

where $\gamma = 0.4$ for equal-mass stars.

2.2.2 Initial conditions

The table 2.2.1 details the initial conditions of each simulation made in this thesis in which all simulations have 10^4 stars. The first column is the number of the simulation, the second column is the initial mass of the stars in solar masses, the third column is the initial radius of the stars in solar radius, the fourth column is the virial radius of the cluster in parsecs, the fifth column is the total mass of the cluster in solar masses, the sixth column is the mass of the gas in solar masses, the seventh column is the radius of the gas in pc and the eighth column is the crossing time in Myr. It is important to mention that the initial radii and masses are from the paper of (Windhorst et al., 2018) and the stars in the clusters have the same mass and radius initially.

ID	$M_{\rm star}$ [$M_\odot$]	$R_{\rm star}$ [$R_\odot$]	$R_{\rm v}$ [pc]	$M_{\rm cluster}$ [$M_\odot$]	$M_{\rm gas}$ [$M_\odot$]	$R_{\rm gas}$ [pc]	$t_{\rm cross}$ [Myr]
1	15	1.51	0.05	3×10^5	1.5×10^5	0.05	2.1×10^{-4}
2	30	2.12	0.05	6×10^5	3×10^5	0.05	1.5×10^{-4}
3	50	2.86	0.05	1×10^6	5×10^5	0.05	1.1×10^{-4}
4	100	4.12	0.05	2×10^6	1×10^6	0.05	8.0×10^{-5}
5	15	1.51	0.05	1.5×10^5	—	—	4.3×10^{-4}
6	30	2.12	0.05	3×10^5	—	—	3.0×10^{-4}
7	50	2.86	0.05	5×10^5	—	—	2.3×10^{-4}
8	100	4.12	0.05	1×10^6	—	—	1.6×10^{-4}
9	15	1.51	0.1	3×10^5	1.5×10^5	0.1	6.0×10^{-4}
10	30	2.12	0.1	6×10^5	3×10^5	0.1	4.3×10^{-4}
11	50	2.86	0.1	1×10^6	5×10^5	0.1	3.3×10^{-4}
12	100	4.12	0.1	2×10^6	1×10^6	0.1	2.3×10^{-4}
13	15	1.51	0.1	1.5×10^5	—	—	1.2×10^{-3}
14	30	2.12	0.1	3×10^5	—	—	8.6×10^{-4}
15	50	2.86	0.1	5×10^5	—	—	6.6×10^{-4}
16	100	4.12	0.1	1×10^6	—	—	4.7×10^{-4}
17	15	1.51	0.5	3×10^5	1.5×10^5	0.5	6.5×10^{-3}
18	30	2.12	0.5	6×10^5	3×10^5	0.5	4.8×10^{-3}
19	50	2.86	0.5	1×10^6	5×10^5	0.5	3.7×10^{-3}
20	100	4.12	0.5	2×10^6	1×10^6	0.5	2.6×10^{-3}
21	15	1.51	0.5	1.5×10^5	—	—	1.3×10^{-2}
22	30	2.12	0.5	3×10^5	—-	—	9.6×10^{-3}
23	50	2.86	0.5	5×10^5	—	—	7.4×10^{-3}
24	100	4.12	0.5	1×10^6	—	—	5.2×10^{-3}

Table 2.2.1: Initial conditions of the simulations.

2.3 Collision treatment

The stellar collision condition used is:

$$r \leq R_1 + R_2, \tag{2.3.1}$$

where r is the distance between both stars center of mass and R_1 and R_2 are the radii of the stars. A collision occurs when two stars are separated by a distance equal to or smaller than the sum of their radii, which also means that they are in physical contact. When this condition is reached, then both stars are replaced by a new star whose total mass is the sum of the masses of the stars before the collision. Thus, the new star assumes the same density as the previously merging

stars.

The mass and radius of the new star are given by the following equations

$$M_{\text{new}} = M_1 + M_2, \tag{2.3.2}$$

$$R_{\text{new}} = R_1 \left(\frac{M_1 + M_2}{M_1} \right)^{1/3}, \tag{2.3.3}$$

where M_1 and M_2 are the mass of the two stars.

The initial mass of the cluster M_{cluster} is related to the number of stars N and the mass of the star M_{star}

$$M_{\text{star}} = M_{\text{cluster}}/N \tag{2.3.4}$$

The total mass of the cluster with an external potential is calculated as

$$M_{\text{tot}} = M_{\text{stars}} + M_{\text{ext}}. \tag{2.3.5}$$

Chapter 3

Analysis

3.1 Pop. III star cluster simulations

In this work, we run 24 simulations, and the evolution of all the clusters in our sample evolved up to 10 Myr to be able to be analyzed later in the mass versus radius diagrams. All clusters simulated here have a total of 10^4 stars and in each cluster, the mass of the external potentials is equal to the mass in stars ($M_{\rm ext} = M_{\rm stars}$). Analyzing the clusters to which we included a background potential, we noticed that they have in common that regardless of their initial conditions, only a single star escapes at the end of their evolution of these. It is important to note that the words 'very massive stars' are included in the following descriptions because the evolution of these clusters shows single collisions (a single collision at different times with different objects within the cluster).
For the simulations 17, 18, 19, and 20 (ID 17, ID 18, ID 19, and ID 20) do not dominate collisions ($t_{\rm coll} > t_{\rm relax}$) which does not result in the formation of a most massive object but rather the formation of several very massive stars (since the single collisions are not with the same object). These clusters have in common that they have an external potential and that they have a virial radius of $R_{\rm v} =$ 0.5 pc. ID17 has a mass in the cluster of $M_{\rm cluster} = 3 \times 10^5$ M$_\odot$, with each star having a mass equal to $M_{\rm star} = 15$ M$_\odot$, a stellar radius of $R_{\rm star} = 1.51$ R$_\odot$ and an external potential of $M_{\rm gas} = 1.5 \times 10^5$ M$_\odot$. ID 18 has a mass of the cluster equal to $M_{\rm cluster} = 6 \times 10^5$ M$_\odot$, with each star having a mass equal to $M_{\rm star} = 30$ M$_\odot$, a stellar radius of $R_{\rm star} = 2.12$ R$_\odot$ and an external potential of $M_{\rm gas} = 3 \times 10^5$ M$_\odot$. For ID 19 the total mass of the cluster is equal to $M_{\rm cluster} = 1 \times 10^6$ M$_\odot$,

with each star having a mass equal to $M_{\rm star} = 50$ M$_\odot$, a radius of $R_{\rm star} = 2.86$ R$_\odot$ and an external potential of $M_{\rm gas} = 5 \times 10^5$ M$_\odot$. ID 20 has a mass of this cluster equal to $M_{\rm cluster} = 2 \times 10^6$ M$_\odot$, with each star having a mass equal to $M_{\rm star} = 100$ M$_\odot$, a radius of $R_{\rm star} = 4.12$ R$_\odot$ and an external potential of $M_{\rm gas} = 1 \times 10^6$ M$_\odot$. All these simulations have in common that within a cluster that is mostly stable with horizontal Lagrangian radii lines with a slight expansion of the cluster for the different percentages of enclosed mass.

The following set of simulations 9, 10, 11, and 12 (ID 9, ID 10, ID 11, and ID 12) have a virial radius equal to $R_{\rm v} = 0.1$ pc and also an external potential. ID 9 has stars of equal mass of $M_{\rm star} = 15$ M$_\odot$, a radius of $R_{\rm star} = 1.51$ R$_\odot$, a total mass of the cluster of $M_{\rm cluster} = 3 \times 10^5$ M$_\odot$ and an external potential of $M_{\rm gas} = 1.5 \times 10^5$ M$_\odot$. ID 10 has stars of equal mass of $M_{\rm star} = 30$ M$_\odot$, radius of $R_{\rm star} = 2.12$ R$_\odot$, a total mass of the cluster of $M_{\rm cluster} = 6 \times 10^5$ M$_\odot$ and an external potential of $M_{\rm gas} = 3 \times 10^5$ M$_\odot$. ID 11 has stars of equal mass of $M_{\rm star} = 50$ M$_\odot$, a radius of $R_{\rm star} = 2.86$ R$_\odot$, a total mass of the cluster of $M_{\rm cluster} = 1 \times 10^6$ M$_\odot$ and an external potential of $M_{\rm gas} = 5 \times 10^5$ M$_\odot$. The cluster in ID 12 has stars of an equal mass of $M_{\rm star} = 100$ M$_\odot$, a radius of $R_{\rm star} = 4.12$ R$_\odot$, a total mass of the cluster of $M_{\rm cluster} = 2 \times 10^6$ M$_\odot$ and an external potential of $M_{\rm gas} = 1 \times 10^6$ M$_\odot$. The mass of the most massive object for ID 9 achieves a mass of 2775 M$_\odot$ after the collapse at ~ 6 Myr, for ID 10 achieves a mass of 13920 M$_\odot$ after the collapse ~ 4 Myr, in ID 11 it reaches a mass of 33700 M$_\odot$ where there is a collapse between 2.5 and 3.5 Myr and the cluster in ID 12 reaches a mass of 96100 M$_\odot$ with a collapse at ~ 2 Myr. In all this set of simulations, there is an expansion of the lagrangian radii for 10%, 50%, and 90% of the enclosed mass after only one collapse during its evolution.

In figure 3.1.1, we show simulation number 2 (ID2) with an external potential where the collapse of the cluster occurs between 1 and 2 Myr. In those times, the largest number of collisions in the cluster occurs, which makes the mass of the massive object grow up to 26190 M$_\odot$. In the simulations with potential, a clear delay in the collapse of the cluster is seen in the work previously done by Reinoso et al. (2020) which makes the crossing time vary by 0.5 in the specific case that the mass of the external potential and the total mass in stars are equal inside the cluster compared to simulations without this external potential. This delay is mainly due to the increase in the kinetic energy of the stars within the cluster, which makes the gravitational collapse take a little longer to occur. This is more

visible when analyzing the simulations with and without the potential for the same physical parameters. The Lagrangian radii show us that after the collapse there is an expansion of the cluster at 10%, 50%, and 90% of the enclosed mass.

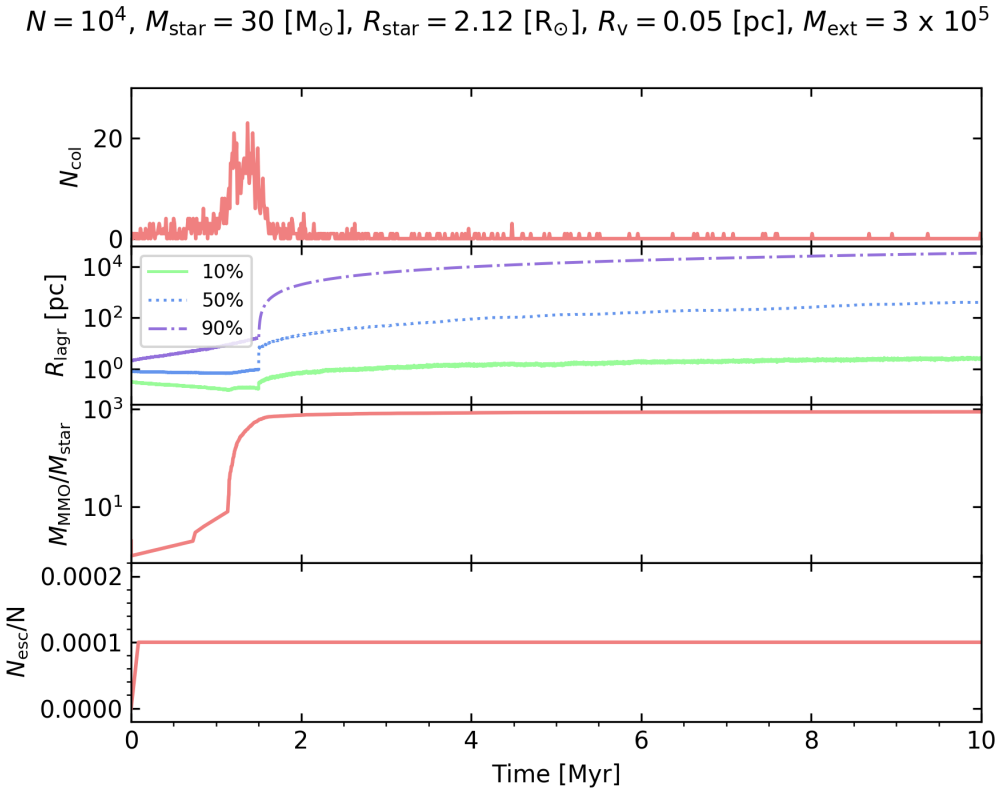

Figure 3.1.1: Evolution of a star cluster with 10^4 stars with an external potential of the same mass. Each star in the cluster has the same mass and radius of 30 $M_\odot$ and 2.12 $R_\odot$, respectively. The virial radius is 0.05 pc and the cluster has evolved to 10 Myr. The *first panel* shows the number of collisions over time, the *second panel* shows the evolution of the Lagrangian radii of the cluster at 10%, 50% and 90% of the enclosed mass, the *third panel* shows the mass of the most massive object in the cluster divided by the initial mass of each star and the *last panel* shows the number of escaping stars divided by the total number of stars. Source: Kirsty L.K. Sehlke-Abarca et. al. in preparation.

With the same virial radius $R_v = 0.05$ pc and with a background potential are the simulations number 1 (ID 1), number 3 (ID 3), and number 4 (ID 4). ID 1 has stars of equal mass of $M_{star} = 15$ $M_\odot$, a radius of $R_{star} = 1.51$ $R_\odot$, a total mass of the cluster of $M_{cluster} = 3 \times 10^5$ $M_\odot$ and an external potential of $M_{gas} = 1.5 \times 10^5$ $M_\odot$. ID 3 has stars of equal mass of $M_{star} = 50$ $M_\odot$, a radius of $R_{star} = 2.86$ $R_\odot$, a total mass of the cluster of $M_{cluster} = 1 \times 10^6$ $M_\odot$ and an external potential of

$M_{\rm gas} = 5 \times 10^5$ M$_\odot$. The densest simulation of this work is ID 4 which has stars of an equal mass of $M_{\rm star} = 100$ M$_\odot$, a radius of $R_{\rm star} = 4.12$ R$_\odot$, a total mass of the cluster of $M_{\rm cluster} = 2 \times 10^6$ M$_\odot$ and has an external potential of $M_{\rm gas} = 1 \times 10^6$ M$_\odot$. These clusters reach a mass of the most massive object of 11385 M$_\odot$ collapsing at ~ 2 Myr for ID 1, 59600 M$_\odot$ for ID 3 collapsing at ~ 1 Myr and a mass of 171400 M$_\odot$ for the densest cluster ID 4 that a collapse takes place between 0 and 1 Myr. The ID 1 cluster shows an expansion of the Lagrangian radii for 10%, 50%, and 90% of the enclosed mass while for ID 3 and ID 4, there is a collapse of the innermost layer shown via the 10% line and an expansion of the outermost layers such as the 50% and 90% line of the enclosed mass.

For the simulations 21, 22, 23, and 24 (ID 21, ID 22, ID 23, and ID 24) do not dominate collisions ($t_{\rm coll} > t_{\rm relax}$). Clusters in this sample that do not have a background potential and have a viral radius of $R_{\rm v} = 0.5$ pc are described below. The only simulations in which there was no very massive object were simulations number 21 and 22 (ID 21 and ID 22) since there are no collisions in these clusters. In these cases, the cluster expands slightly with some escaping stars being 13 and 27 respectively. ID 21 has a total mass of $M_{\rm cluster} = 1.5 \times 10^5$ M$_\odot$, stars of equal mass of $M_{\rm star} = 15$ M$_\odot$ and stellar radii of $R_{\rm star} = 1.51$ R$_\odot$ and ID 22 has a total mass of $M_{\rm cluster} = 3 \times 10^5$ M$_\odot$, stars of equal mass of $M_{\rm star} = 30$ M$_\odot$ and stellar radii of $R_{\rm star} = 2.12$ R$_\odot$. For simulation number 23 (ID 23) there are few collisions and very massive stars are formed. This cluster is expanding slightly and the stars escaping is about 55. It should be noted that this cluster is characterized by having a total mass of $M_{\rm cluster} = 5 \times 10^5$ M$_\odot$, stars of an equal mass of $M_{\rm star} = 50$ M$_\odot$ and stellar radii of $R_{\rm star} = 2.86$ R$_\odot$. Finally, in simulation number 24 (ID 24) there are few collisions and very massive stars are formed. This cluster is also expanding slightly and the stars escaping is about 132. It should be noted that this cluster is characterized by having a total mass of $M_{\rm cluster} = 1 \times 10^6$ M$_\odot$, stars of an equal mass of $M_{\rm star} = 100$ M$_\odot$ and radius of $R_{\rm star} = 4.12$ R$_\odot$.

The following set of simulations 13, 14, 15, and 16 (ID 13, ID 14, ID 15, and ID 16) has a viral radius of $R_{\rm v} = 0.1$ pc and do not have a background potential. The collapse of ID 13 occurs at ~ 2.5 Myr, in which the total mass of the cluster is $M_{\rm cluster} = 1.5 \times 10^5$ M$_\odot$, stars of an equal mass of $M_{\rm star} = 15$ M$_\odot$ and radius of $R_{\rm star} = 1.51$ R$_\odot$. The mass of the most massive object reaches 5895 M$_\odot$ and stars equal to 826 escape from the cluster, therefore a mass of 131715 M$_\odot$ remains in the cluster. The collapse of ID 14 occurs at ~ 1.5 Myr, in which the total

mass of the cluster is $M_{\rm cluster} = 3 \times 10^5$ $M_\odot$, stars of an equal mass of $M_{\rm star} = 30$ $M_\odot$ and radius of $R_{\rm star} = 2.12$ $R_\odot$. The mass of the most massive object reaches 16200 $M_\odot$ and stars equal to 1078 escapes from the cluster, therefore a mass of 251460 $M_\odot$ remains in the cluster. The collapse of ID 15 occurs at ~ 1 Myr, in which the total mass of the cluster is $M_{\rm cluster} = 5 \times 10^5$ $M_\odot$, stars of an equal mass of $M_{\rm star} = 50$ $M_\odot$ and radius of $R_{\rm star} = 2.86$ $R_\odot$. The mass of the most massive object reaches 33650 $M_\odot$ and stars equal to 1326 escapes from the cluster, therefore a mass of 400050 $M_\odot$ remains in the cluster. The collapse of ID 16 occurs before 1 Myr. Here the total mass of the cluster is $M_{\rm cluster} = 1 \times 10^6$ $M_\odot$, stars of equal mass of $M_{\rm star} = 100$ $M_\odot$ and stellar radii of $R_{\rm star} = 4.12$ $R_\odot$. The mass of the most massive object reaches 89900 $M_\odot$ and stars equal to 1604 escapes from the cluster, therefore a mass of 749700 $M_\odot$ remains in the cluster. In all these simulations there is also an expansion of the outer layers of the Lagrangian radii that encompass the enclosed mass at 50% and 90% of the enclosed mass.
In figure 3.1.2, we show simulation number 6 (ID6). As mentioned above for these simulations the collapse occurs earlier, in this case before 1 Myr. The number of collisions in this simulation is higher than in the simulation shown in the previous figure. This makes the growth of the central object much faster until 28800 $M_\odot$. A collapse of the shell at 10% of the Lagrangian radius and an expansion of the shells for 50% and 90% are shown. The amount of stars that escape in simulations without potential is much higher than those that escape in simulations with potential with 1981 stars.

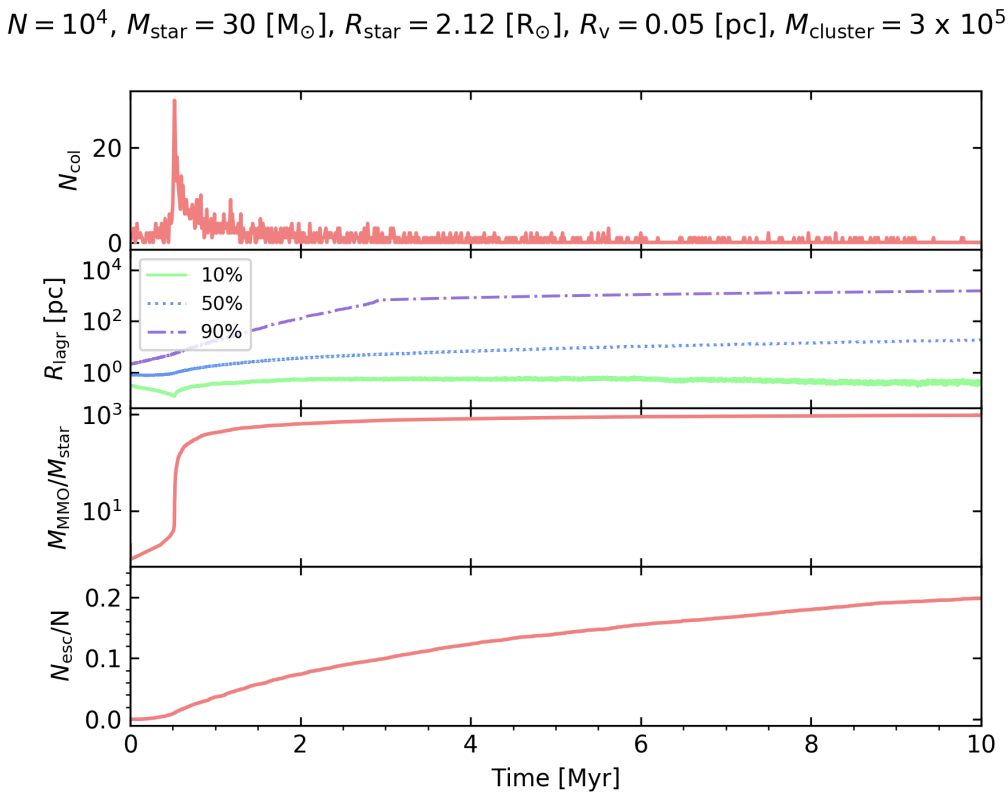

Figure 3.1.2: Evolution of a star cluster of 10^4 stars without an external potential, each star in the cluster has the same mass and radius 30 $M_\odot$ and 2.12 $R_\odot$, respectively. The virial radius is 0.05 pc and the cluster has evolved to 10 Myr. The *first panel* shows the number of collisions over time, the *second panel* shows the evolution of the Lagrangian radii of the cluster at 10%, 50% and 90% of the mass, the *third panel* shows the mass of the most massive object in the cluster divided by the initial mass of each star and the *last panel* shows the number of escaping stars divided by the total number of stars. Source: Kirsty L.K. Sehlke-Abarca et. al. in preparation.

With the same virial radius $R_v = 0.05$ pc and without a background potential are the simulations number 5 (ID 5), number 7 (ID 7), and number 8 (ID 8). ID 5 has stars of an equal mass of $M_{star} = 15$ $M_\odot$, a radius of $R_{star} = 1.51$ $R_\odot$ and a total mass of the cluster of $M_{cluster} = 1.5 \times 10^5$ $M_\odot$ reaching a mass of the most massive object of 12195 $M_\odot$ and stars equal to 1633 escape from the cluster, therefore a mass of 113310 $M_\odot$ remains in the cluster. The collapse of the cluster occurs before 1 Myr and after that, there is an expansion of the lagrangian radii lines for 50% and 90% of the enclosed mass. ID 7 which has stars of an equal mass of $M_{star} = 50$ $M_\odot$, a stellar radius of $R_{star} = 2.86$ $R_\odot$ and a total mass of the cluster of $M_{cluster} = 5 \times 10^5$ $M_\odot$ reaching a mass of the most massive object of 55900 $M_\odot$

and stars equal to 2304 escape from the cluster, therefore a mass of 328900 $M_\odot$ remains in the cluster. The collapse of the cluster occurs before 1 Myr and there is a first collapse of the innermost layer and then a second collapse deeper also for 10% of the Lagrangian radius and expansion in the outermost layers for 50% and 90% of the Lagrangian radii of the enclosed mass. On the other hand, ID 8 which contains stars of an equal mass of $M_{\rm star} = 100$ $M_\odot$, a radius of $R_{\rm star} = 4.12$ $R_\odot$ and a total mass of the cluster of $M_{\rm cluster} = 1 \times 10^6$ $M_\odot$ reaching a mass of the most massive object of 138200 $M_\odot$ and stars equal to 2672 escape from the cluster, therefore a mass of 594600 $M_\odot$ remains in the cluster. The collapse of the cluster occurs before 1 Myr and there is a first collapse of the innermost layer and then a second collapse deeper also for 10% of the Lagrangian radius and expansion in the outermost layers for 50% and 90% of the Lagrangian radii of the enclosed mass.

3.2 Theoretical results for Pop. III star clusters

In figure 3.2.1 the theoretical results of the simulations for 1Myr can be observed. To make the following three figures, other parameters like the effective cross-section, the Safronov number, and velocity dispersion which are defined later were considered in the initial (Escala, 2021) equations, which causes a change in the figures. For a better understanding, I will rewrite the initial equations with the new parameters in consideration for equation 1.5.2. Star clusters that have $t_{\rm coll} \leq t_{\rm H}$ are unable to expand before the onset of runaway collisions, they will probably collapse towards the formation of an MMO:

$$M \geq \left(\frac{4\pi M_{\rm star}}{3\Sigma_0 t_{\rm H} G^{1/2}} \right)^{2/3} R^{7/3}, \tag{3.2.1}$$

where $M_{\rm star}$ is the mass of a single star, Σ_0 is the effective cross section, $t_{\rm H}$ is the age of the system and G is the gravitational constant. The effective cross section Σ_0 is defined as $\Sigma_0 = 16\sqrt{\pi} R_{star}^2 (1+\Theta)$, where $R_{\rm star}$ is the radius of a single star and Θ is the Safronov number $\Theta = 9.54((M_{star}\ {\rm R}_\odot)/(\ {\rm M}_\odot R_{\rm star}))((100\ {\rm km\,s^{-1}})/\sigma))^2$. σ is the velocity dispersion of a virialized system $\sigma = \sqrt{GM/R}$, where M is the total mass and R the characteristic radius of the system.

On the other hand, how Pop. III star clusters (PSCs) that have $t_{\rm relax} \leq t_{\rm H}$ will expand their effective radius before collisions become important, moving its

position to the collisional stable region:

$$R \leq [((t_{\rm H} M_{\rm star})/0.1) \ln (M/M_{\rm star})]^{2/3} (G/M)^{1/3} . \tag{3.2.2}$$

From the figures 3.2.1, 3.2.2 and 3.2.3 we can see that if we consider longer times the conditions for the solid lines and the segmented ones move from left to right which means that clusters with a smaller virial radius are more unstable, forming most massive objects more quickly.

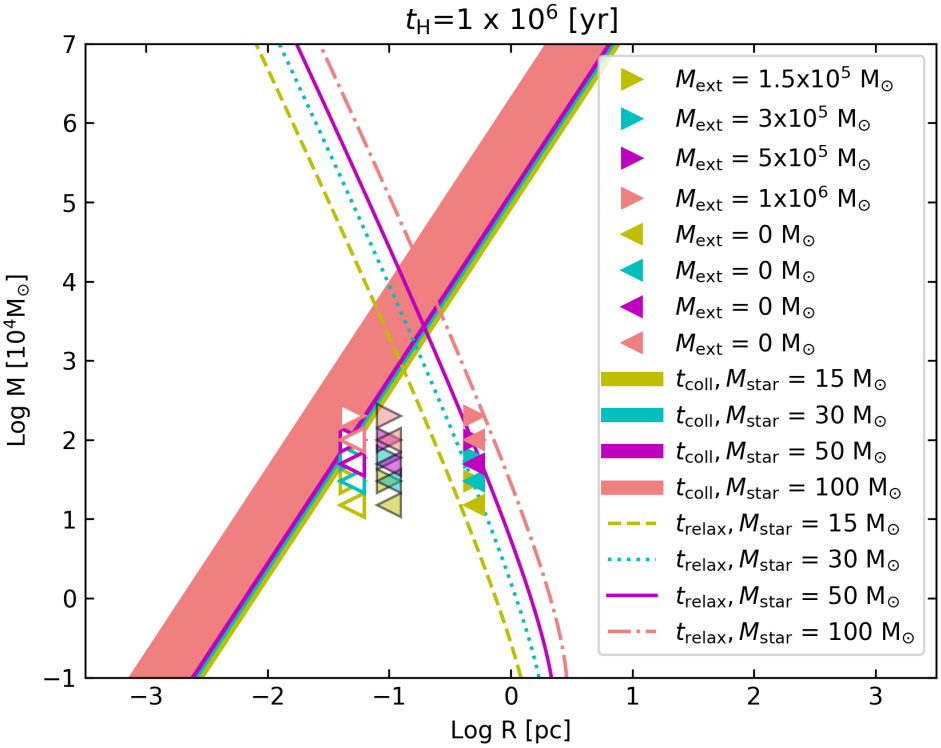

Figure 3.2.1: In this figure the radius of the cluster in pc is shown on the x-axis while on the y-axis is the mass of the cluster in $M_\odot$. The different colors in the figure represent the different initial stellar masses for both triangles and lines. In this case, yellow represents the initial mass of each star of 15 $M_\odot$, cyan represents the initial mass of each star of 30 $M_\odot$, magenta represents an initial mass of each star of 50 $M_\odot$ and finally coral represents an initial mass of each star of 100 $M_\odot$. Triangles pointing to the right ($\triangleright$) represent simulations with an external potential on the other hand triangles pointing to the left ($\triangleleft$) represent simulations without an external potential. The solid lines are from the condition of equation 3.2.1 for the different σ associated with the initial conditions, while the dashed lines are from equation 3.2.2 both for a time evolution of 1 Myr. Source: Kirsty L.K. Sehlke-Abarca et. al. in preparation.

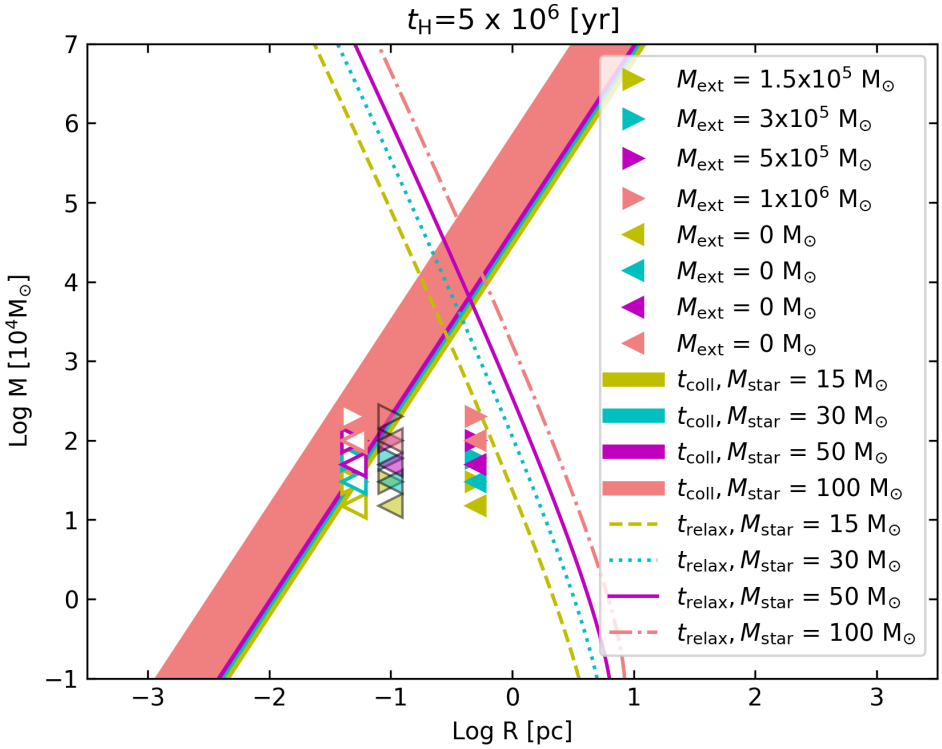

Figure 3.2.2: In this figure the radius of the cluster in pc is shown on the x-axis while on the y-axis is shown the mass of the cluster in $M_\odot$. The different colors in the figure represent the different initial stellar masses for both triangles and lines, in this case, yellow represents an initial mass of each star of 15 $M_\odot$, cyan represents an initial mass of each star of 30 $M_\odot$, magenta represents an initial mass of each star of 50 $M_\odot$ and finally coral represents an initial mass of each star of 100 $M_\odot$. Triangles pointing to the right ($\triangleright$) represent simulations with an external potential on the other hand triangles pointing to the left ($\triangleleft$) represent simulations without an external potential. The solid lines are from the condition of equation 3.2.1 for the different σ associated with the initial conditions, while the dashed lines are from equation 3.2.2 both for a time evolution of 5 Myr. Source: Kirsty L.K. Sehlke-Abarca et. al. in preparation.

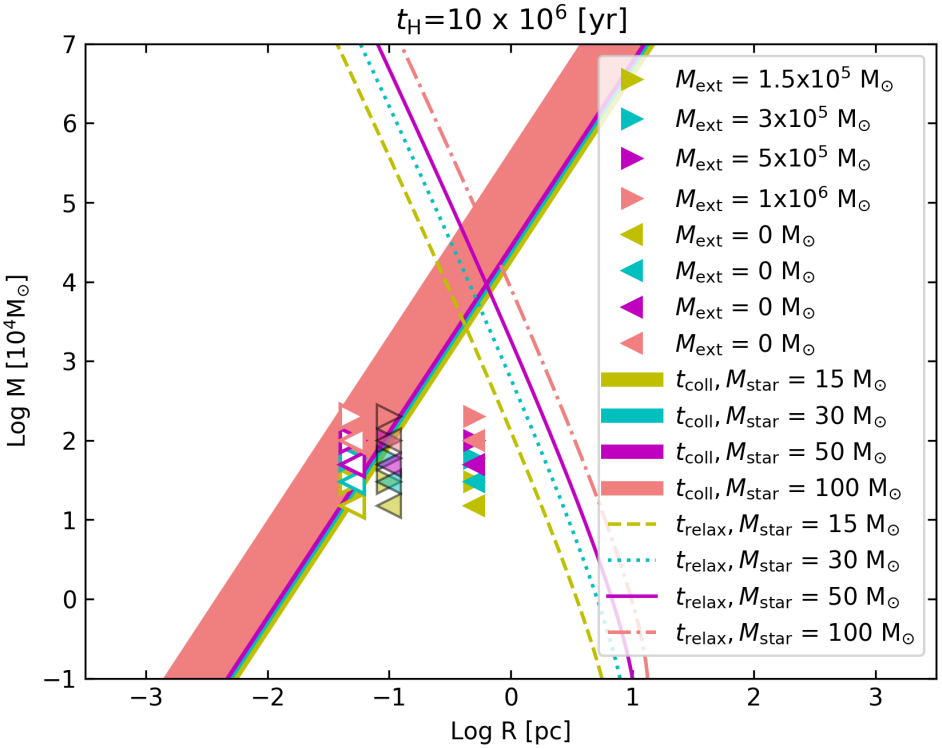

Figure 3.2.3: In this figure the radius of the cluster in pc is shown on the x-axis while on the y-axis is shown the mass of the cluster in $M_\odot$. The different colors in the figure represent the different initial stellar masses for both triangles and lines, in this case, yellow represents an initial mass of each star of 15 $M_\odot$, cyan represents an initial mass of each star of 30 $M_\odot$, magenta represents an initial mass of each star of 50 $M_\odot$ and finally coral represents an initial mass of each star of 100 $M_\odot$. Triangles pointing to the right ($\triangleright$) represent simulations with an external potential on the other hand triangles pointing to the left ($\triangleleft$) represent simulations without an external potential. The solid lines are from the condition of equation 3.2.1 for the different σ associated with the initial conditions, while the dashed lines are from equation 3.2.2 both for a time evolution of 10 Myr. Source: Kirsty L.K. Sehlke-Abarca et. al. in preparation.

3.3 Efficiencies for Pop. III star clusters

In figures 3.3.1, 3.3.2 and 3.3.3 showing the efficiencies for the formation of most massive objects we have that the x-axis shows the initial stellar mass of the cluster $M_{\rm ini}$ divided by the critical mass $M_{\rm crit}$ and in the y-axis the efficiency

$\epsilon_{\rm MMO}$ of each simulation. We have

$$M_{\rm ini} = M_{\rm PSC,final} + M_{\rm MMO} + M_{esc}, \tag{3.3.1}$$

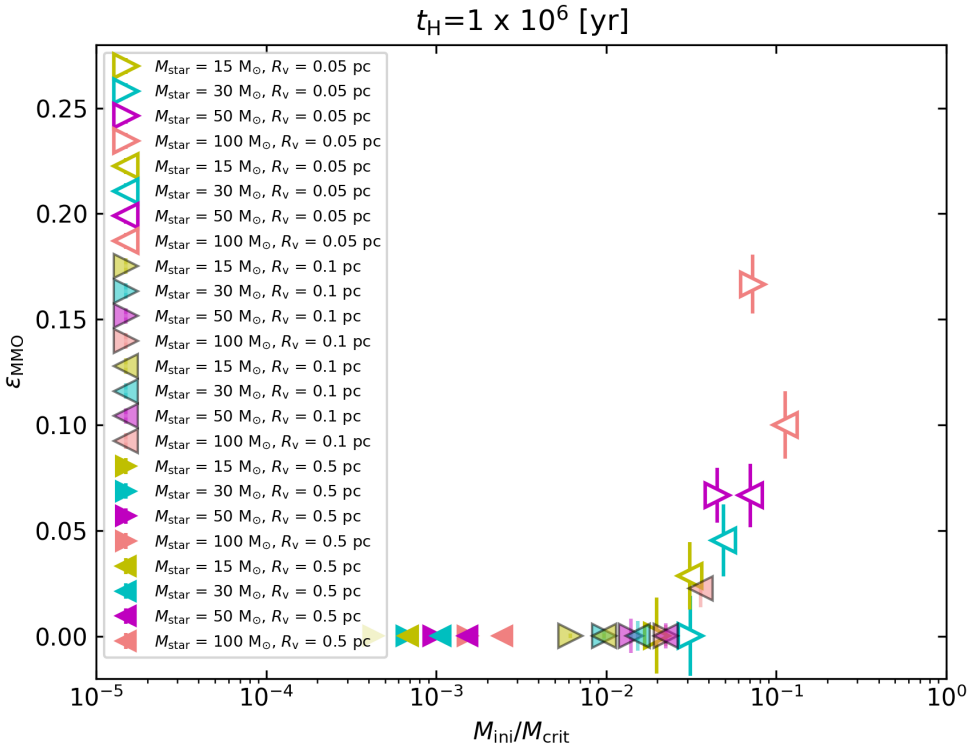

Figure 3.3.1: Efficiencies at which MMOs are formed calculated with equation 3.3.3. The x-axis shows the initial stellar mass of the cluster $M_{\rm ini}$ divided by the critical mass $M_{\rm crit}$ until 1 Myr. Source: Kirsty L.K. Sehlke-Abarca et. al. in preparation.

where $M_{\rm PSC,final}$ is the mass of the Pop. III star cluster remaining at the end of the simulation, $M_{\rm MMO}$ is the mass of the most massive object and M_{esc} is the mass of the stars escaping from the cluster. Here we consider that the mass of the central massive object is equal to $M_{\rm CMO} = M_{\rm PSC} + M_{\rm MMO}$.

On the other hand, the critical mass $M_{\rm crit}$ is obtained from the condition given by the equation 3.2.1:

$$M_{\rm crit} = \left(\frac{4\pi M_{\rm star}}{3\Sigma_0 t_{\rm H} G^{1/2}}\right)^{2/3} R^{7/3}. \tag{3.3.2}$$

The efficiency $\epsilon_{\rm MMO}$ is obtained from the same equation used in (Escala, 2021),

$$\epsilon_{\rm MMO} = \left(1 + \frac{M_{\rm PSC}}{M_{\rm MMO}}\right)^{-1}, \tag{3.3.3}$$

where the mass of the PSC is calculated as $M_{\rm PSC} = (1 - \epsilon_{\rm MMO})M_{\rm CMO}$ and the mass of the MMO can be calculated as $M_{\rm MMO} = \epsilon_{\rm MMO} M_{\rm CMO}$.
From here we notice that the simulations in which we do not add a background potential have a higher efficiency than when we consider this background potential for the same physical conditions of the cluster. The highest efficiencies are reached for denser and more massive clusters which reach a value of $\sim 20\%$.

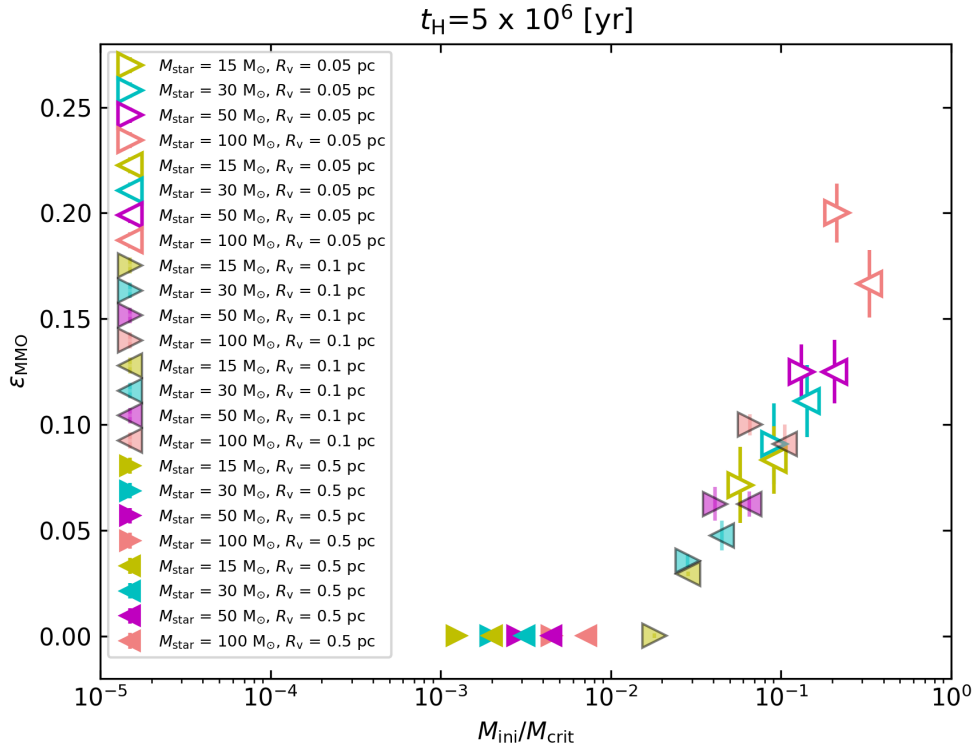

Figure 3.3.2: Efficiencies at which MMOs are formed calculated with equation 3.3.3. The x-axis shows the initial stellar mass of the cluster $M_{\rm ini}$ divided by the critical mass $M_{\rm crit}$ until 5 Myr. Source: Kirsty L.K. Sehlke-Abarca et. al. in preparation.

It is important to note that the mass of the background potential was only considered in the simulations and not in the subsequent calculations of the efficiencies since this potential only affects the dynamics of the cluster and does

not directly contribute to the growth of the most massive object to be considered in efficiency.

The error bars are associated with the average of three simulations for the same single configuration with a different random seed to obtain the statistics of the simulations.

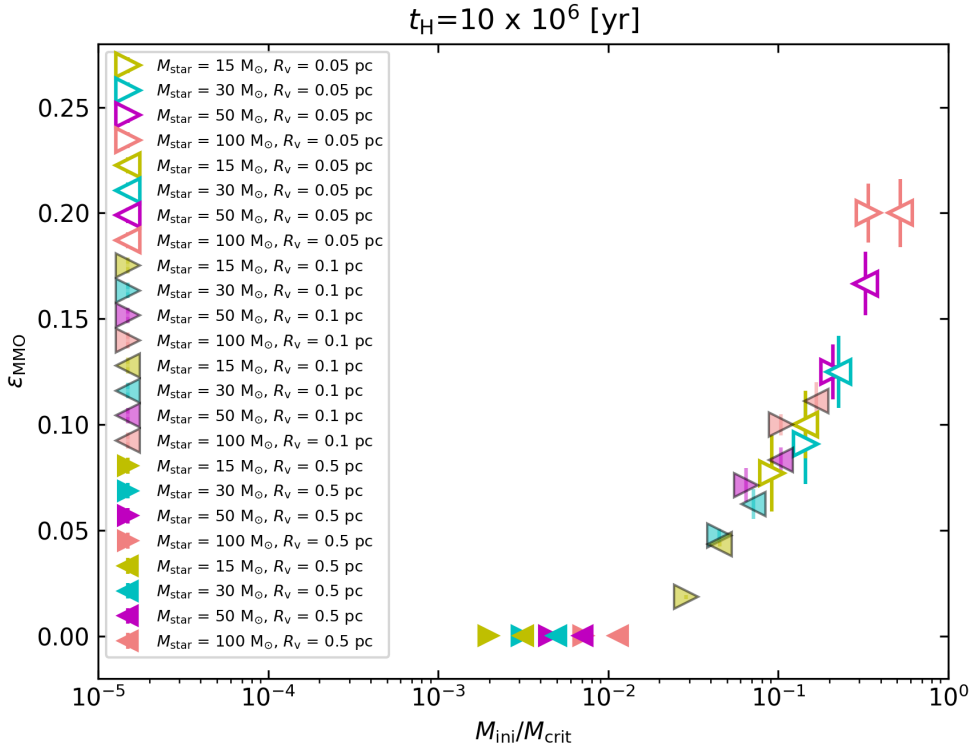

Figure 3.3.3: Efficiencies at which MMOs are formed calculated with equation 3.3.3. The x-axis shows the initial stellar mass of the cluster M_{ini} divided by the critical mass M_{crit} until 10 Myr. Source: Kirsty L.K. Sehlke-Abarca et. al. in preparation.

The highest efficiencies at 10 Myr are obtained from simulations ID4 and ID8 which include the densest and most massive clusters, which reach efficiencies 20 %, since these simulations are located close, in the radius versus mass diagram, to the line that describes the condition ($t_{coll} \leq t_H$) where collisions dominate. The ID7 simulation reaches 16.6 %. A 12.5 % in efficiency is obtained from the ID3 and ID6 simulations. The ID5 simulation reaches a 10 % in efficiency. A little further down the ID2 simulation has 9.09 % in efficiency. Finally, for simulations with a virial radius R_v of 0.05 pc, the ID1 simulation achieves 7.69 % in efficiency.

For simulations with a virial radius $R_{\rm v}$ of 0.1 pc, the ID16 simulation reaches 11.1 % in efficiency. A 10 % in efficiency is obtained by the ID12 simulation. The ID15 simulation has an 8.33 % in efficiency. 7.14 % is obtained from the initial conditions of the ID11 simulation. The ID14 simulation reaches 6.25 %. The ID10 and ID13 simulations have efficiencies of 4.76 % and 4.34 % respectively. And finally, 1.85 % is obtained by the ID9 simulation.
The efficiencies of the ID17, ID18, ID19, ID20, ID21, ID22, ID23, ID24 simulations are very close to 0 % for virial radius $R_{\rm v}$ of 0.5 pc. These last simulations are located close, in the radius versus mass diagram, to the line that describes the condition ($t_{\rm relax} \leq t_{\rm H}$) where collisions do not dominate.

3.4 Summary of the main results

In the following tables 3.4.1,3.4.2 and 3.4.3 we can summarize the main results of the simulations for 1 Myr, 5 Myr, and 10 Myr.

ID	M_{MMO} [$\mathrm{M}_\odot$]	N_{esc}	M_{PSC} [$\mathrm{M}_\odot$]	M_{CMO} [$\mathrm{M}_\odot$]
1	30	1	149955	149985
2	60	1	299910	299970
3	33100	1	466850	499950
4	150300	1	849600	999900
5	4155	209	142710	146865
6	12660	364	276420	289080
7	31450	492	443950	475400
8	88400	712	840400	928800
9	30	1	149955	149985
10	60	1	299910	299970
11	100	1	499850	499950
12	200	1	999700	999900
13	30	10	149820	149850
14	60	27	299130	299190
15	100	65	496650	496750
16	22000	186	959400	981400
17	30	0	149970	150000
18	60	0	299940	300000
19	100	0	499900	500000
20	200	0	999800	1000000
21	0	0	149985	149985
22	0	0	299970	299970
23	50	1	499900	499950
24	100	1	999800	999900

Table 3.4.1: Main results from the simulations at 1 Myr.

ID	$M_{\rm MMO}$ [$M_\odot$]	$N_{\rm esc}$	$M_{\rm PSC}$ [$M_\odot$]	$M_{\rm CMO}$ [$M_\odot$]
1	10650	1	139335	149985
2	25470	1	274500	299970
3	59300	1	440650	499950
4	168800	1	831100	999900
5	10815	1077	123030	133845
6	25920	1397	232170	258090
7	51000	1709	363550	414550
8	130100	1990	670900	801000
9	30	1	149955	149985
10	10530	1	289440	299970
11	30600	1	469350	499950
12	91400	1	908500	999900
13	4200	467	138795	142995
14	12810	675	266940	279750
15	27600	858	429500	457100
16	77500	1048	817700	895200
17	30	1	149955	149985
18	60	1	299910	299970
19	100	1	499850	499950
20	200	1	999700	999900
21	0	3	149940	149940
22	0	6	299790	299790
23	50	13	499300	499350
24	200	24	997400	997600

Table 3.4.2: Main results from the simulations at 5 Myr.

ID	$M_{\rm MMO}$ [$M_\odot$]	$N_{\rm esc}$	$M_{\rm PSC}$ [$M_\odot$]	$M_{\rm CMO}$ [$M_\odot$]
1	11385	1	138600	149985
2	26190	1	273780	299970
3	59600	1	440350	499950
4	171400	1	828500	999900
5	12195	1633	113310	125505
6	28800	1981	211770	240570
7	55900	2304	328900	384800
8	138200	2672	594600	732800
9	2775	1	147210	149985
10	13920	1	286050	299970
11	33700	1	466250	499950
12	96100	1	903800	999900
13	5895	826	131715	137610
14	16200	1078	251460	267660
15	33650	1326	400050	433700
16	89900	1604	749700	839600
17	30	1	149955	149985
18	60	1	299910	299970
19	100	1	499850	499950
20	200	1	999700	999900
21	0	13	149790	149790
22	0	27	299160	299160
23	100	55	497150	497250
24	200	132	986600	986800

Table 3.4.3: Main results from the simulations at 10 Myr.

Chapter 4

Discussion

This research provides support for the hypothesis that the scenario from Reinoso et al. (2020) works in Pop. III clusters above the critical mass limit. Nonetheless, there are several caveats, as we currently do not even know the mass range and the typical mass-radius relation for Pop. III clusters, so that some very important questions are open. Also the initial mass function of the Pop. III stars is unclear, the binary fraction, and other factors. It is important to acknowledge these uncertainties more specifically. Even though we do not know exactly what the radii of these Pop. III star clusters would be, we know from the study of parameters that we did that the smaller the radius of this cluster is, the more massive will be the object that will form in its center and therefore the efficiencies will be much higher. This leads us to the fact that Pop. III star clusters more massive than 1×10^6 $M_\odot$ would have efficiencies greater than 20 % to form massive objects in their center. It should be noted that the processes of formation of structures in the universe are much more complex than just including the dynamics of bodies within a system, but it is already a good start to include more physical processes that interact with our main system in the future and check those only collisions have a high contribution in the formation process. The formation of structures in the early universe was also shaped by processes such as accretion, fragmentation, rotation, initial mass function, and the reionization of hydrogen, among others that should be considered for a complete analysis of the formation of black holes. As detailed above we take a simplified case of stellar clusters where we do not consider stellar evolution and all the stars in the cluster have the same mass and radius. The background potential that we

included in some of our simulations helped us to understand that although we would be modeling the effects of the gas within the cluster, it would not have a greater effect on the total mass of the most massive object at the same time, since as previously studied by Reinoso et al. (2020) simulations with a background potential could double the total mass of the most massive objects but in a much longer time. It would make sense that for denser simulations than those carried out in this investigation, they would be studied up to 1 Myr since by then they would have already formed a most massive object in their center since simulations that we made less dense for that time had not yet reached the collapse of the cluster. In the end, this is what we seek to answer as such massive structures were formed in such a short time.

From the figure 3.2.3 clusters in the left side of the solid lines fulfill the condition $t_{\rm coll} \leq t_{\rm H}$ or $t_{\rm relax} \leq t_{\rm H}$. Clusters at 0.5 pc are in the stable region ($t_{\rm relax} \leq t_{\rm coll}$) and the clusters at 0.1 pc and 0.05 pc, although they are in the stability region, are almost on the edge of the instability region, where collisions are increasingly greater crossing the unstable line ($t_{\rm coll} \leq t_{\rm relax}$). As mentioned in (Escala, 2021) there is a mass limit of $\sim 4 \times 10^8$ $M_\odot$ where all the mass turns into a central massive object. It is to be expected that simulations with masses of Pop. III star clusters similar to the latter and bigger would allow us to see this jump in efficiencies between 0 and 1. For now, with the results already obtained, we can only see how the efficiency starts at 0 and slowly these efficiencies increase. Bearing this in mind, our results are in agreement with previous works and follow a very similar line.

On the other hand, we only know their characteristics theoretically about population III stars, so we will have to wait to corroborate this information in the future, which seems quite promising. In the future, we will have access to supercomputers that allow us to make much more massive and compact simulations, which will help us to analyze the collisions within these systems to calculate how these efficiencies increase. This together with other works that are being done in parallel will give us access to larger samples to be able to analyze our graphs to have a considerable sample and achieve more general conclusions. This added to what the promising images of the James Webb Space Telescope (JWST) can say in the observational counterpart and of course future space telescopes that allow us to observe the early universe such as some of them: Transient High-Energy Sky and Early Universe Surveyor (THESEUS), JWST,

Extremely Large Telescope (ELT), Square Kilometre Array (SKA), Wide-Field Infrared Survey Telescope (WFIRST), EUCLID, European Extremely Large Telescope (E-ELT), Giant Magellan Telescope (GMT), Thirty Meter Telescope (TMT) and Laser Interferometer Space Antenna (LISA) among others, which has us waiting for what we can observe.

Chapter 5

Conclusion

In this investigation, therefore, support has been shown with numerical methods of a new path for the formation of massive black holes theoretically proposed by (Escala, 2021) to those previously proposed (Rees, 1984) and (Volonteri, 2010). Our sample of simulations is a simplified case of star clusters of equal mass and radius where half of our simulations have an external background potential with a plummer profile (Plummer, 1911) and the other do not. Some of these simulations after the simulation started to show an instability that causes a massive central object to form in the center of these clusters through collisions. This is called the coexistence of nuclear star clusters and black holes and it has been proposed that they formed in the same way but that they have different evolutionary mechanisms. Our systems, being located in the early universe, have masses and radii of population III stars, which are characterized by being very massive. The characteristics of these stars were taken from (Windhorst et al., 2018). We do not include stellar evolution in our calculations since our aim here is to investigate dynamical processes taking place before even the most massive main-sequence stars in the cluster have evolved. The simulations were made using NBODY6++ to study the dynamics of N bodies with an extension for parallel computers designed by (Spurzem, 1999). Our main results indicate that, on the one hand, the efficiencies we obtained are not so high due to the mass-radius relationship used for the stars. Even though Population III stars are very massive, the radii used are small, which means that in the dynamics of the stars in the cluster they have a smaller cross-section than if they had larger radii and the cross-section had a greater range of stars moving within the cluster which would cause greater

collisions, a more massive central object and therefore greater efficiencies. And on the other hand, all our simulations with external potential have a delay that had already been studied by (Reinoso et al., 2020) but now we consider characteristic parameters of population III stars, this means that the kinetic energy of the system is higher than when we do not consider this potential and the collapse of the cluster takes time to occur in addition to this the system is more compact and very few stars escape from the cluster.

Research has recently been carried out that also explores this new scenario for the formation of black holes such as those of (Vergara et al., 2022b) and (Vergara et al., 2022a) finding that the most massive objects reach masses of approximately $10^4 - 10^5$ $M_\odot$ and the highest black hole formation efficiency is almost 50 % of the stellar mass at the end of the simulation.

Three important uncertainty to consider are: first, to be able to use the initial mass function (IMF) of primordial stars. This type of work has been studied by (Hartwig et al., 2015), in which it is detailed that they constrain the lower-mass limit of the (Pop III) IMF with the total number of stars in large, unbiased surveys of the Milky Way and they conclude that the lower mass IMF limit is 0.65 $M_\odot$ with a confidence of 95 % and that the Pop III star formation rate peaks at z $\sim$ 20 and that each successfully Pop III forming halo has an average stellar mass content of $\sim$ 100 $M_\odot$. It would be interesting to be able to add to our simulations the IMF of the stars of Pop. III to be able to analyze how our results vary in these cases. Another uncertainty to consider in the future is the rotation of Pop. III star clusters. In studies of (Vergara et al., 2021) it was found that rotation seems to affect the collision rate by at most 20 % and that rotation helps to retain more stars in the system, reducing the number of escapers by a factor of $2 - 3$ depending on the model and the specific realization. The third uncertainty is if still gas would be present in these clusters and how it affects the evolution. This has been studied in (Boekholt et al., 2018) where it is demonstrated that the interplay between stellar dynamics, gas accretion, and protostellar evolution is particularly relevant increasing collisions from 0.1-1% of the initial population to about 10% when compared to gas-free models. This is because gas accretion onto the protostars enhances their radii, which causes an enhanced collisional cross section eventually causing major collisions inside the cluster.

With the first images of a black hole so far (Event Horizon Telescope Collaboration et al., 2019) and (Collaboration et al., 2022) we are expectant to see what future

generations of telescopes have to show us in the coming years such as the SKA, WFIRST, EUCLID, JWST, and large ground-based facilities such as E-ELTs, GMT, and TMT (Dijkstra, 2019) among others as THESEUS or detections of other ways to study the early universe like the one found in (Bowman et al., 2018) where they report the detection of a flattened absorption profile in the sky-averaged radio spectrum, which is centered at a frequency of 78 megahertz and has a best-fitting full- width at half-maximum of 19 megahertz and an amplitude of 0.5 kelvin to study the early universe. Another way in which they are working to study these objects is with LISA, which is planned to be launched in the early 2030s where they will explore the possibility of discovering seed black holes and track their growth across all cosmic epochs, by detecting the gravitational wave signal they emit at the time of their coalescence, i.e. they pair to form close binaries. Gravitational waves travel unimpeded through the cosmos and carry information on the masses and spins of the merging black holes. To this purpose they introduce key concepts on the gravitational wave emission from binaries, describing briefly their formation pathway during halo-halo mergers and galaxy collisions (Colpi, 2019).

Bibliography

Aarseth, S. J. (1963). Dynamical evolution of clusters of galaxies, i. *Monthly Notices of the Royal Astronomical Society*, 126:223.

Aarseth, S. J. (1985). Direct methods for N-body simulations. In *Multiple time scales*, pages 377–418.

Aarseth, S. J. (1999). From NBODY1 to NBODY6: The Growth of an Industry. , 111(765):1333–1346.

Aarseth, S. J. (2001). NBODY2: A direct N-body integration code. , 6(5):277–291.

Ahmad, A. and Cohen, L. (1973). A numerical integration scheme for the n-body gravitational problem. *Journal of Computational Physics*, 12(3):389–402.

Alister Seguel, P. J., Schleicher, D. R. G., Boekholt, T. C. N., Fellhauer, M., and Klessen, R. S. (2020). Formation of SMBH seeds in Population III star clusters through collisions: the importance of mass loss. *MNRAS*, 493(2):2352–2362.

Begelman, M. and Rees, M. (2009). *Gravity's Fatal Attraction: Black Holes in the Universe*. Cambridge University Press, 2 edition.

Boekholt, T. C. N., Schleicher, D. R. G., Fellhauer, M., Klessen, R. S., Reinoso, B., Stutz, A. M., and Haemmerlé, L. (2018). Formation of massive seed black holes via collisions and accretion. *MNRAS*, 476(1):366–380.

Bowman, J. D., Rogers, A. E. E., Monsalve, R. A., Mozdzen, T. J., and Mahesh, N. (2018). An absorption profile centred at 78 megahertz in the sky-averaged spectrum. *Nature*, 555(7694):67–67–70.

Bromm, V. (2013a). Formation of the first stars. *Reports on Progress in Physics*, 76(11):112901.

Bromm, V. (2013b). The first stars and galaxies - Basic principles. *Asociacion Argentina de Astronomia La Plata Argentina Book Series*, 4:3.

Bromm, V., Kudritzki, R. P., and Loeb, A. (2001). Generic spectrum and ionization efficiency of a heavy initial mass function for the first stars. *The Astrophysical Journal*, 552(2):464–472.

Collaboration, E. H. T., Akiyama, K., Alberdi, A., Alef, W., Algaba, J. C., Anantua, R., Asada, K., Azulay, R., Bach, U., Baczko, A.-K., Ball, D., Baloković,

M., Barrett, J., Bauböck, M., Benson, B. A., Bintley, D., Blackburn, L., Blundell, R., Bouman, K. L., Bower, G. C., Boyce, H., Bremer, M., Brinkerink, C. D., Brissenden, R., Britzen, S., Broderick, A. E., Broguiere, D., Bronzwaer, T., Bustamante, S., Byun, D.-Y., Carlstrom, J. E., Ceccobello, C., Chael, A., kwan Chan, C., Chatterjee, K., Chatterjee, S., Chen, M.-T., Chen, Y., Cheng, X., Cho, I., Christian, P., Conroy, N. S., Conway, J. E., Cordes, J. M., Crawford, T. M., Crew, G. B., Cruz-Osorio, A., Cui, Y., Davelaar, J., Laurentis, M. D., Deane, R., Dempsey, J., Desvignes, G., Dexter, J., Dhruv, V., Doeleman, S. S., Dougal, S., Dzib, S. A., Eatough, R. P., Emami, R., Falcke, H., Farah, J., Fish, V. L., Fomalont, E., Ford, H. A., Fraga-Encinas, R., Freeman, W. T., Friberg, P., Fromm, C. M., Fuentes, A., Galison, P., Gammie, C. F., García, R., Gentaz, O., Georgiev, B., Goddi, C., Gold, R., Gómez-Ruiz, A. I., Gómez, J. L., Gu, M., Gurwell, M., Hada, K., Haggard, D., Haworth, K., Hecht, M. H., Hesper, R., Heumann, D., Ho, L. C., Ho, P., Honma, M., Huang, C.-W. L., Huang, L., Hughes, D. H., Ikeda, S., Impellizzeri, C. M. V., Inoue, M., Issaoun, S., James, D. J., Jannuzi, B. T., Janssen, M., Jeter, B., Jiang, W., Jiménez-Rosales, A., Johnson, M. D., Jorstad, S., Joshi, A. V., Jung, T., Karami, M., Karuppusamy, R., Kawashima, T., Keating, G. K., Kettenis, M., Kim, D.-J., Kim, J.-Y., Kim, J., Kim, J., Kino, M., Koay, J. Y., Kocherlakota, P., Kofuji, Y., Koch, P. M., Koyama, S., Kramer, C., Kramer, M., Krichbaum, T. P., Kuo, C.-Y., Bella, N. L., Lauer, T. R., Lee, D., Lee, S.-S., Leung, P. K., Levis, A., Li, Z., Lico, R., Lindahl, G., Lindqvist, M., Lisakov, M., Liu, J., Liu, K., Liuzzo, E., Lo, W.-P., Lobanov, A. P., Loinard, L., Lonsdale, C. J., Lu, R.-S., Mao, J., Marchili, N., Markoff, S., Marrone, D. P., Marscher, A. P., Martí-Vidal, I., Matsushita, S., Matthews, L. D., Medeiros, L., Menten, K. M., Michalik, D., Mizuno, I., Mizuno, Y., Moran, J. M., Moriyama, K., Moscibrodzka, M., Müller, C., Mus, A., Musoke, G., Myserlis, I., Nadolski, A., Nagai, H., Nagar, N. M., Nakamura, M., Narayan, R., Narayanan, G., Natarajan, I., Nathanail, A., Fuentes, S. N., Neilsen, J., Neri, R., Ni, C., Noutsos, A., Nowak, M. A., Oh, J., Okino, H., Olivares, H., Ortiz-León, G. N., Oyama, T., Özel, F., Palumbo, D. C. M., Paraschos, G. F., Park, J., Parsons, H., Patel, N., Pen, U.-L., Pesce, D. W., Piétu, V., Plambeck, R., PopStefanija, A., Porth, O., Pötzl, F. M., Prather, B., Preciado-López, J. A., Psaltis, D., Pu, H.-Y., Ramakrishnan, V., Rao, R., Rawlings, M. G., Raymond, A. W., Rezzolla, L., Ricarte, A., Ripperda, B., Roelofs, F., Rogers, A., Ros, E., Romero-Cañizales, C., Roshanineshat, A., Rottmann, H., Roy, A. L., Ruiz, I., Ruszczyk, C., Rygl, K. L. J., Sánchez, S., Sánchez-Argüelles, D., Sánchez-Portal, M., Sasada, M., Satapathy, K., Savolainen, T., Schloerb, F. P., Schonfeld, J., Schuster, K.-F., Shao, L., Shen, Z., Small, D., Sohn, B. W., SooHoo, J., Souccar, K., Sun, H., Tazaki, F., Tetarenko, A. J., Tiede, P., Tilanus, R. P. J., Titus, M., Torne, P., Traianou, E., Trent, T., Trippe, S., Turk, M., van Bemmel, I., van Langevelde, H. J., van Rossum, D. R., Vos, J., Wagner, J., Ward-Thompson, D., Wardle, J., Weintroub, J., Wex, N., Wharton, R., Wielgus, M., Wiik, K., Witzel, G., Wondrak, M. F., Wong, G. N., Wu, Q., Yamaguchi, P., Yoon, D., Young, A., Young, K., Younsi, Z., Yuan, F., Yuan, Y.-F., Zensus, J. A., Zhang, S., Zhao, G.-Y., Zhao, S.-S., Agurto, C., Allardi, A., Amestica, R., Araneda,

J. P., Arriagada, O., Berghuis, J. L., Bertarini, A., Berthold, R., Blanchard, J., Brown, K., Cárdenas, M., Cantzler, M., Caro, P., Castillo-Domínguez, E., Chan, T. L., Chang, C.-C., Chang, D. O., Chang, S.-H., Chang, S.-C., Chen, C.-C., Chilson, R., Chuter, T. C., Ciechanowicz, M., Colin-Beltran, E., Coulson, I. M., Crowley, J., Degenaar, N., Dornbusch, S., Durán, C. A., Everett, W. B., Faber, A., Forster, K., Fuchs, M. M., Gale, D. M., Geertsema, G., González, E., Graham, D., Gueth, F., Halverson, N. W., Han, C.-C., Han, K.-C., Hasegawa, Y., Hernández-Rebollar, J. L., Herrera, C., Herrero-Illana, R., Heyminck, S., Hirota, A., Hoge, J., Schimpf, S. R. H., Howie, R. E., Huang, Y.-D., Jiang, H., Jinchi, H., John, D., Kimura, K., Klein, T., Kubo, D., Kuroda, J., Kwon, C., Lacasse, R., Laing, R., Leitch, E. M., Li, C.-T., Liu, C.-T., Liu, K.-Y., Lin, L. C.-C., Lu, L.-M., Mac-Auliffe, F., Martin-Cocher, P., Matulonis, C., Maute, J. K., Messias, H., Meyer-Zhao, Z., Montaña, A., Montenegro-Montes, F., Montgomerie, W., Nolasco, M. E. M., Muders, D., Nishioka, H., Norton, T. J., Nystrom, G., Ogawa, H., Olivares, R., Oshiro, P., Pérez-Beaupuits, J. P., Parra, R., Phillips, N. M., Poirier, M., Pradel, N., Qiu, R., Raffin, P. A., Rahlin, A. S., Ramírez, J., Ressler, S., Reynolds, M., Rodríguez-Montoya, I., Saez-Madain, A. F., Santana, J., Shaw, P., Shirkey, L. E., Silva, K. M., Snow, W., Sousa, D., Sridharan, T. K., Stahm, W., Stark, A. A., Test, J., Torstensson, K., Venegas, P., Walther, C., Wei, T.-S., White, C., Wieching, G., Wijnands, R., Wouterloot, J. G. A., Yu, C.-Y., (), W. Y., and Zeballos, M. (2022). First sagittarius a* event horizon telescope results. i. the shadow of the supermassive black hole in the center of the milky way. *The Astrophysical Journal Letters*, 930(2):L12.

Colpi, M. (2019). Probing the formation of the seeds of supermassive black holes with gravitational waves. In Latif, M. and Schleicher, D., editors, *Formation of the First Black Holes*, pages 241–268.

Das, A., Schleicher, D. R. G., Leigh, N. W. C., and Boekholt, T. C. N. (2021). Formation of supermassive black hole seeds in nuclear star clusters via gas accretion and runaway collisions. *MNRAS*, 503(1):1051–1069.

Dijkstra, M. (2019). Prospects for detecting the first black holes with the next generation of telescopes. In Latif, M. and Schleicher, D., editors, *Formation of the First Black Holes*, pages 269–288.

Escala, A. (2021). Observational Support for Massive Black Hole Formation Driven by Runaway Stellar Collisions in Galactic Nuclei. *ApJ*, 908(1):57.

Event Horizon Telescope Collaboration, Akiyama, K., Alberdi, A., Alef, W., Asada, K., Azulay, R., Baczko, A.-K., Ball, D., Baloković, M., Barrett, J., Bintley, D., Blackburn, L., Boland, W., Bouman, K. L., Bower, G. C., Bremer, M., Brinkerink, C. D., Brissenden, R., Britzen, S., Broderick, A. E., Broguiere, D., Bronzwaer, T., Byun, D.-Y., Carlstrom, J. E., Chael, A., Chan, C.-k., Chatterjee, S., Chatterjee, K., Chen, M.-T., Chen, Y., Cho, I., Christian, P., Conway, J. E., Cordes, J. M., Crew, G. B., Cui, Y., Davelaar, J., De Laurentis, M., Deane, R., Dempsey, J., Desvignes, G., Dexter, J., Doeleman,

S. S., Eatough, R. P., Falcke, H., Fish, V. L., Fomalont, E., Fraga-Encinas, R., Freeman, W. T., Friberg, P., Fromm, C. M., Gómez, J. L., Galison, P., Gammie, C. F., García, R., Gentaz, O., Georgiev, B., Goddi, C., Gold, R., Gu, M., Gurwell, M., Hada, K., Hecht, M. H., Hesper, R., Ho, L. C., Ho, P., Honma, M., Huang, C.-W. L., Huang, L., Hughes, D. H., Ikeda, S., Inoue, M., Issaoun, S., James, D. J., Jannuzi, B. T., Janssen, M., Jeter, B., Jiang, W., Johnson, M. D., Jorstad, S., Jung, T., Karami, M., Karuppusamy, R., Kawashima, T., Keating, G. K., Kettenis, M., Kim, J.-Y., Kim, J., Kim, J., Kino, M., Koay, J. Y., Koch, P. M., Koyama, S., Kramer, M., Kramer, C., Krichbaum, T. P., Kuo, C.-Y., Lauer, T. R., Lee, S.-S., Li, Y.-R., Li, Z., Lindqvist, M., Liu, K., Liuzzo, E., Lo, W.-P., Lobanov, A. P., Loinard, L., Lonsdale, C., Lu, R.-S., MacDonald, N. R., Mao, J., Markoff, S., Marrone, D. P., Marscher, A. P., Martí-Vidal, I., Matsushita, S., Matthews, L. D., Medeiros, L., Menten, K. M., Mizuno, Y., Mizuno, I., Moran, J. M., Moriyama, K., Moscibrodzka, M., Müller, C., Nagai, H., Nagar, N. M., Nakamura, M., Narayan, R., Narayanan, G., Natarajan, I., Neri, R., Ni, C., Noutsos, A., Okino, H., Olivares, H., Ortiz-León, G. N., Oyama, T., Özel, F., Palumbo, D. C. M., Patel, N., Pen, U.-L., Pesce, D. W., Piétu, V., Plambeck, R., PopStefanija, A., Porth, O., Prather, B., Preciado-López, J. A., Psaltis, D., Pu, H.-Y., Ramakrishnan, V., Rao, R., Rawlings, M. G., Raymond, A. W., Rezzolla, L., Ripperda, B., Roelofs, F., Rogers, A., Ros, E., Rose, M., Roshanineshat, A., Rottmann, H., Roy, A. L., Ruszczyk, C., Ryan, B. R., Rygl, K. L. J., Sánchez, S., Sánchez-Arguelles, D., Sasada, M., Savolainen, T., Schloerb, F. P., Schuster, K.-F., Shao, L., Shen, Z., Small, D., Sohn, B. W., SooHoo, J., Tazaki, F., Tiede, P., Tilanus, R. P. J., Titus, M., Toma, K., Torne, P., Trent, T., Trippe, S., Tsuda, S., van Bemmel, I., van Langevelde, H. J., van Rossum, D. R., Wagner, J., Wardle, J., Weintroub, J., Wex, N., Wharton, R., Wielgus, M., Wong, G. N., Wu, Q., Young, K., Young, A., Younsi, Z., Yuan, F., Yuan, Y.-F., Zensus, J. A., Zhao, G., Zhao, S.-S., Zhu, Z., Algaba, J.-C., Allardi, A., Amestica, R., Anczarski, J., Bach, U., Baganoff, F. K., Beaudoin, C., Benson, B. A., Berthold, R., Blanchard, J. M., Blundell, R., Bustamente, S., Cappallo, R., Castillo-Domínguez, E., Chang, C.-C., Chang, S.-H., Chang, S.-C., Chen, C.-C., Chilson, R., Chuter, T. C., Córdova Rosado, R., Coulson, I. M., Crawford, T. M., Crowley, J., David, J., Derome, M., Dexter, M., Dornbusch, S., Dudevoir, K. A., Dzib, S. A., Eckart, A., Eckert, C., Erickson, N. R., Everett, W. B., Faber, A., Farah, J. R., Fath, V., Folkers, T. W., Forbes, D. C., Freund, R., Gómez-Ruiz, A. I., Gale, D. M., Gao, F., Geertsema, G., Graham, D. A., Greer, C. H., Grosslein, R., Gueth, F., Haggard, D., Halverson, N. W., Han, C.-C., Han, K.-C., Hao, J., Hasegawa, Y., Henning, J. W., Hernández-Gómez, A., Herrero-Illana, R., Heyminck, S., Hirota, A., Hoge, J., Huang, Y.-D., Impellizzeri, C. M. V., Jiang, H., Kamble, A., Keisler, R., Kimura, K., Kono, Y., Kubo, D., Kuroda, J., Lacasse, R., Laing, R. A., Leitch, E. M., Li, C.-T., Lin, L. C. C., Liu, C.-T., Liu, K.-Y., Lu, L.-M., Marson, R. G., Martin-Cocher, P. L., Massingill, K. D., Matulonis, C., McColl, M. P., McWhirter, S. R., Messias, H., Meyer-Zhao, Z., Michalik, D., Montaña, A., Montgomerie, W., Mora-Klein, M., Muders, D., Nadolski, A., Navarro, S.,

Neilsen, J., Nguyen, C. H., Nishioka, H., Norton, T., Nowak, M. A., Nystrom, G., Ogawa, H., Oshiro, P., Oyama, T., Parsons, H., Paine, S. N., Peñalver, J., Phillips, N. M., Poirier, M., Pradel, N., Primiani, R. A., Raffin, P. A., Rahlin, A. S., Reiland, G., Risacher, C., Ruiz, I., Sáez-Madaín, A. F., Sassella, R., Schellart, P., Shaw, P., Silva, K. M., Shiokawa, H., Smith, D. R., Snow, W., Souccar, K., Sousa, D., Sridharan, T. K., Srinivasan, R., Stahm, W., Stark, A. A., Story, K., Timmer, S. T., Vertatschitsch, L., Walther, C., Wei, T.-S., Whitehorn, N., Whitney, A. R., Woody, D. P., Wouterloot, J. G. A., Wright, M., Yamaguchi, P., Yu, C.-Y., Zeballos, M., Zhang, S., and Ziurys, L. (2019). First M87 Event Horizon Telescope Results. I. The Shadow of the Supermassive Black Hole. , 875(1):L1.

Greene, J. E., Strader, J., and Ho, L. C. (2020). Intermediate-mass black holes. *Annual Review of Astronomy and Astrophysics*, 58(1):257–312.

Grisdale, K., Thatte, N., Devriendt, J., Pereira-Santaella, M., Slyz, A., Kimm, T., Dubois, Y., and Yi, S. K. (2021). Predicting the observability of population III stars with ELT-HARMONI via the helium 1640 Å emission line. *MNRAS*, 501(4):5517–5537.

Gurkan, M. A., Freitag, M., and Rasio, F. A. (2004). Formation of massive black holes in dense star clusters. i. mass segregation and core collapse. *The Astrophysical Journal*, 604(2):632–652.

Haemmerlé, L., Woods, T. E., Klessen, R. S., Heger, A., and Whalen, D. J. (2018). The evolution of supermassive Population III stars. *MNRAS*, 474(2):2757–2773.

Hartwig, T., Bromm, V., Klessen, R. S., and Glover, S. C. O. (2015). Constraining the primordial initial mass function with stellar archaeology. , 447(4):3892–3908.

Inayoshi, K., Visbal, E., and Haiman, Z. (2020). The assembly of the first massive black holes. *Annual Review of Astronomy and Astrophysics*, 58(1):27–97.

Kashlinsky, A. (2021). Cosmological Advection Flows in the Presence of Primordial Black Holes as Dark Matter and Formation of First Sources. *Physical Review Letters*, 126(1):011101.

Khalisi, E., Wang, L., and Spurzem, R. (2019). NBODY6++ Manual for the Computer Code.

Klessen, R. (2019). Formation of the first stars. In Latif, M. and Schleicher, D., editors, *Formation of the First Black Holes*, pages 67–97.

Kroupa, P. (2001). On the variation of the initial mass function. *MNRAS*, 322(2):231–246.

Lupi, A., Colpi, M., Devecchi, B., Galanti, G., and Volonteri, M. (2014). Constraining the high-redshift formation of black hole seeds in nuclear star clusters with gas inflows. *MNRAS*, 442(4):3616–3626.

Makino, J. (1991). A modified aarseth code for grape and vector processors. *Publications of the Astronomical Society of Japan*, 43:859–876.

Makino, J. and Aarseth, S. J. (1992). On a hermite integrator with ahmad-cohen scheme for gravitational many-body problems. *Publications of the Astronomical Society of Japan*, 44:141–151.

Mikkola, S. (1997). Numerical Treatment of Small Stellar Systems with Binaries. In Docobo, J. A., Elipe, A., and McAlister, H., editors, *Visual Double Stars : Formation, Dynamics and Evolutionary Tracks*, volume 223 of *Astrophysics and Space Science Library*, page 269.

Murphy, L. J., Groh, J. H., Farrell, E., Meynet, G., Ekström, S., Tsiatsiou, S., Hackett, A., and Martinet, S. (2021). Ionizing photon production of Population III stars: effects of rotation, convection, and initial mass function. *MNRAS*, 506(4):5731–5749.

NASA / WMAP Science Team (2006). TIMELINE OF THE UNIVERSE.

Neumayer, N., Seth, A., and Böker, T. (2020). Nuclear star clusters. *AAPR*, 28(1):4.

Neutsch, W. and Scherer, K. (1992). *Celestial mechanics : an introduction to classical and contemporary methods*.

Plummer, H. C. (1911). On the problem of distribution in globular star clusters. , 71:460–470.

Rees, M. J. (1984). Black Hole Models for Active Galactic Nuclei. , 22:471–506.

Regan, J. A. and Haehnelt, M. G. (2009). Pathways to massive black holes and compact star clusters in pre-galactic dark matter haloes with virial temperatures >~10000K. *MNRAS*, 396(1):343–353.

Reinoso, B., Schleicher, D. R. G., Fellhauer, M., Klessen, R. S., and Boekholt, T. C. N. (2018). Collisions in primordial star clusters. Formation pathway for intermediate mass black holes. *A&A proofs*, 614:A14.

Reinoso, B., Schleicher, D. R. G., Fellhauer, M., Leigh, N. W. C., and Klessen, R. S. (2020). The effects of a background potential in star cluster evolution. A delay in the relaxation time-scale and runaway collision processes. *A&A proofs*, 639:A92.

Sakurai, Y., Yoshida, N., and Fujii, M. S. (2019). Growth of intermediate mass black holes by tidal disruption events in the first star clusters. *MNRAS*, 484(4):4665–4677.

Schaerer, D. (2002). On the properties of massive population III stars and metal-free stellar populations. *A&A proofs*, 382(1):28–42.

Spurzem, R. (1999). Direct N-body Simulations. *Journal of Computational and Applied Mathematics*, 109:407–432.

Stiefel, E., K. P. (1965). Perturbation theory of kepler motion based on spinor regularization. *Journal für die reine und angewandte Mathematik*, 218:204–219.

Tanvir, N. R., Le Floc'h, E., Christensen, L., Caruana, J., Salvaterra, R., Ghirlanda, G., Ciardi, B., Maio, U., D'Odorico, V., Piedipalumbo, E., Campana, S., Noterdaeme, P., Graziani, L., Amati, L., Bagoly, Z., Balázs, L. G., Basa, S., Behar, E., De Cia, A., Della Valle, M., De Pasquale, M., Frontera, F., Gomboc, A., Götz, D., Horvath, I., Hudec, R., Mereghetti, S., O'Brien, P. T., Osborne, J. P., Paltani, S., Rosati, P., Sergijenko, O., Stanway, E. R., Szécsi, D., Toth, L. V., Urata, Y., Vergani, S., and Zane, S. (2021). Exploration of the high-redshift universe enabled by THESEUS. *Experimental Astronomy*, 52(3):219–244.

Vergara, M. C., Escala, A., Schleicher, D. R. G., and Reinoso, B. (2022a). Global instability by runaway collisions in nuclear stellar clusters: Numerical tests of a route for massive black hole formation. *arXiv e-prints*, page arXiv:2209.15066.

Vergara, M. Z. C., Escala, A., Schleicher, D. R. G., and Reinoso, B. (2022b). Runaways collisions in nuclear stellar clusters. *Boletin de la Asociacion Argentina de Astronomia La Plata Argentina*, 63:118–120.

Vergara, M. Z. C., Schleicher, D. R. G., Boekholt, T. C. N., Reinoso, B., Fellhauer, M., Klessen, R. S., and Leigh, N. W. C. (2021). Stellar collisions in flattened and rotating Population III star clusters. , 649:A160.

Volonteri, M. (2010). Formation of supermassive black holes. , 18(3):279–315.

Wang, L., Spurzem, R., Aarseth, S., Nitadori, K., Berczik, P., Kouwenhoven, M. B. N., and Naab, T. (2015). Nbody6++gpu: ready for the gravitational million-body problem. *Monthly Notices of the Royal Astronomical Society*, 450(4):4070–4080.

Windhorst, R. A., Timmes, F. X., Wyithe, J. S. B., Alpaslan, M., Andrews, S. K., Coe, D., Diego, J. M., Dijkstra, M., Driver, S. P., Kelly, P. L., and Kim, D. (2018). On the Observability of Individual Population III Stars and Their Stellar-mass Black Hole Accretion Disks through Cluster Caustic Transits. *ApJs*, 234(2):41.